OPTIMIZING NATURAL CONVECTION FROM A HEAT GENERATING CYLINDER FOR DRY CASK STORAGE APPLICATIONS

by

Corey Everett Clifford

B.S. Chemical Engineering, University of Pittsburgh, 2012

Submitted to the Graduate Faculty of

Swanson School of Engineering in partial fulfillment

of the requirements for the degree of

Master of Science

University of Pittsburgh

2014

UNIVERSITY OF PITTSBURGH

SWANSON SCHOOL OF ENGINEERING

This thesis was presented

by

Corey Everett Clifford

It was defended on

December 20, 2013

and approved by

Mark L. Kimber, PhD, Assistant Professor
Department of Mechanical Engineering and Material Science

David A. Aumiller, PhD, Adjunct Faculty
Department of Mechanical Engineering and Material Science

Anirban Jana, PhD, Senior Scientific Specialist
Pittsburgh Supercomputing Center

Thesis Advisor: Mark L. Kimber, PhD, Assistant Professor
Department of Mechanical Engineering and Material Science

OPTIMIZING NATURAL CONVECTION FROM A HEAT GENERATING CYLINDER FOR DRY CASK STORAGE APPLICATIONS

Corey Everett Clifford, MS

University of Pittsburgh, 2014

Although high-density fuel pool storage provides an acceptable method for housing used fuel assemblies, a number of concerns have triggered a call for the reduction of current fuel pool inventories by mandating a maximum permissible time in which fuel assemblies may be placed in wet storage before transfer to passive, dry storage conditions. In anticipation of an accelerated fuel transfer program, the principal goal of this investigation is to develop a fundamental understanding of the physics associated with the buoyancy-induced flow around dry casks in an effort to improve the heat rejection capability of the overall system. The aim of this investigation is to minimize the amount of active pool cooling necessary by maximizing the thermal capacity of dry storage configurations. The natural convection flow through horizontally-oriented dry cask systems is numerically investigated using the commercial FLUENT software package. A simplified geometry of a heated horizontal cylinder confined between two, vertical adiabatic walls is employed to evaluate the coupled heat and mass transfer. Two different treatments of the cylinder surface are investigated: constant temperature (isothermal) and constant heat flux (isoflux). To quantify the effect of wall distance on the effective heat transfer from the cylinder surface, 18 different confinement ratios are selected in varying increments from 1.125 to 18.0. Each of these geometrical configurations are evaluated at seven distinct Rayleigh numbers ranging from 10^2 to

10^5. Using the largest confinement ratio as a point of comparison, the results of the computational models are validated to within 5% of previously established heat transfer correlations for free cylinders. Maximum values of the surface-averaged Nusselt number are observed at an optimum confinement ratio for each analyzed Rayleigh number. Relative to the pseudo-unconfined cylinder at the largest confinement ratio, a 54.2% improvement in the heat transfer from an isothermal cylinder surface is observed at the optimum wall spacing for the highest analyzed Rayleigh number. Likewise, an analogous improvement of 46.6% is determined for the same conditions with a constant heat flux surface.

Keywords: CFD, decay heat, dry cask storage, heat transfer, natural convection

TABLE OF CONTENTS

LIST OF TABLES

LIST OF FIGURES

NOMENCLATURE

Variable	Description	Units
A	cylinder surface area	m^2
C	confinement ratio	-
c_p	specific heat	$J\ kg^{-1}\ K^{-1}$
D	cylinder diameter	m
g_c	gravitational constant	$m\ s^{-2}$
Ge	Gebhart number	-
Gr	Grashof number	-
h	fluid enthalpy	$J\ kg^{-1}$
H	channel height	m
k	thermal conductivity	$W\ m^{-1}\ K^{-1}$
Nu	Nusselt number	-
p	static pressure	Pa
P	pressure	Pa
Pr	Prandtl number	-
q	dynamic pressure	Pa
q''	surface heat flux	$W\ m^{-2}$
q'''	volumetric heat generation rate	$W\ m^{-3}$
Ra	Rayleigh number	-
T	temperature	K
W	wall distance	m
v	velocity	$m\ s^{-1}$
Y	cylinder surface normal distance	m
z	height above fluid inlet	m

Greek Symbols

Variable	Description	Units
α	thermal diffusivity	$m^2\ s^{-1}$
β	fluid compressibility	K^{-1}
θ	local angle	°
μ	molecular viscosity	Pa s
ν	kinematic viscosity	$m^2\ s^{-1}$
ρ	density	$kg\ m^{-3}$
ϕ	dimensionless temperature	-

Subscripts / Superscripts

Variable	Description	Units
D	confined cylinder surface-averaged parameter	-
eff	model effective parameter	-
f	film temperature evaluation	-
r	radial direction	-
s	cylinder surface parameter	-
x	x-direction	-
y	y-direction	-
θ	tangential direction	-
∞	unconfined cylinder surface-averaged parameter	-
$*$	flux-defined parameter	-

ACKNOWLEDGMENTS

First and foremost, I would like to thank the late Dr. John D. Metzger for believing in me and allowing me to continue my education at the University of Pittsburgh. John was one of my favorite undergraduate and graduate professors at the university and has been sorely missed by all of his students since his passing last October.

I would also like to acknowledge Dr. Mark L. Kimber and the remainder of his talented and knowledgeable research group for their help and guidance over the course of this project. Dr. Kimber graciously stepped in and masterfully served an advisory role in an effort to continue Dr. Metzger's research. Furthermore, I would like to specifically thank Dr. Sagnik Mazumdar for his assistance on the theory and application of CFD techniques throughout this investigation.

Finally, I would like to acknowledge my family and loved ones for their unrelenting support as I continue my schooling at the University of Pittsburgh. Special thanks go to Samantha Culley whom, even after four years, continues to serve as an unwilling reviewer of all my work.

1.0 INTRODUCTION

Nuclear power generation differentiates itself from other forms of energy production due to the nature of its fuel source, both during and following reactor operation. Unlike commercial energy producing plants that utilize the combustion of fossil fuels (coal, natural gas, oil, etc.) as their source of thermal energy generation, nuclear energy is produced via the fission of elements in the actinide series of the periodic table. The fission of heavy atoms such as uranium and plutonium results in the formation of both neutrons, which serve to sustain the chain reaction in the core, and large radioactive nuclides of varying atomic composition. As these fission products are often born in an unstable, radioactive state, they emit gamma and beta radiation in an effort to achieve a more stable configuration.

This gamma and beta energy, more commonly referred to as “decay heat”, results in one of the most significant differences between nuclear energy and other forms of electrical power generation: nuclear energy does not stop being generated after the reaction has been successfully terminated. In fact, immediately following the termination of the nuclear fission chain reaction, the fuel in the core is still producing energy at 6.5% of the full power rate. Although this value may seem trivial relative to the full power level, take, for instance, the Westinghouse AP1000, which is currently rated at 3400 MW of thermal energy with 157 nuclear fuel assemblies. Immediately following shutdown, 221 MW are still being produced within the core, which corresponds to approximately 1.41 MW per fuel assembly. Despite the disparity between the decay

heat energy level and that of full power operation, there is still a tremendous amount of energy being produced, even at a per assembly basis.

Although the initial magnitude of the decay thermal energy present in the used fuel assemblies is quite significant, it is the timeframe at which these powers are present that presents a larger challenge to the nuclear industry. Because some of the unstable fission products produced during nominal reactor operation have half-lives greater than several decades in magnitude, the amount of decay energy present in used nuclear fuel lingers for centuries. To illustrate this slow, monotonic decline in the power level of used nuclear fuel, Figure 1 displays the decay thermal power normalized by the mass of uranium in the fuel from 0.01 to 100 years post-shutdown. Additionally, four different fuel burnups, a measure of how much energy is extracted from the fuel, are presented as a function of time removed from the reactor core.

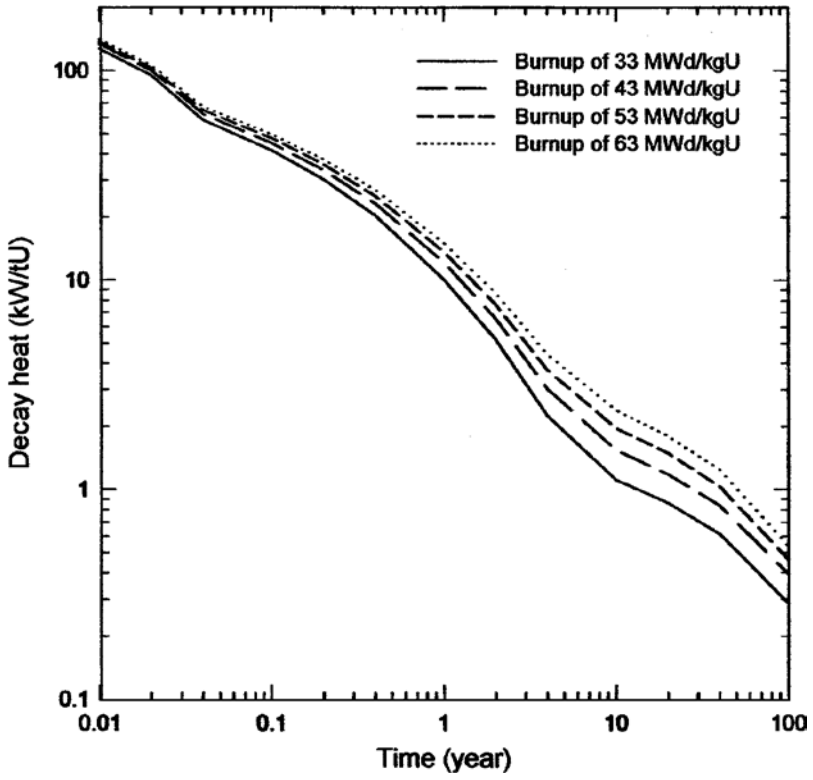

Figure 1: Decay heat distributions from 0.01 to 100 years post-shutdown for used fuel burnups of 33, 43, 53, and 63 MWd / kg U [1]

In an effort to counter the enormous decay energy densities associated with used nuclear fuel, operators transfer the spent fuel assemblies to fuel storage pools after their stint in the reactor core. Within the storage pools, hundreds of fuel assemblies are arranged in storage racks submerged beneath approximately 30 feet of water, which functions as both a coolant and a radiation shield to protect workers during fuel maneuver procedures. Once the thermal energy is transferred from the used fuel assemblies to the coolant, the water is actively pumped from the pool through a heat exchanger where the energy can be discharged in a final, radiation-free coolant stream. An example of an archetypical used nuclear fuel pool is displayed in Figure 2.

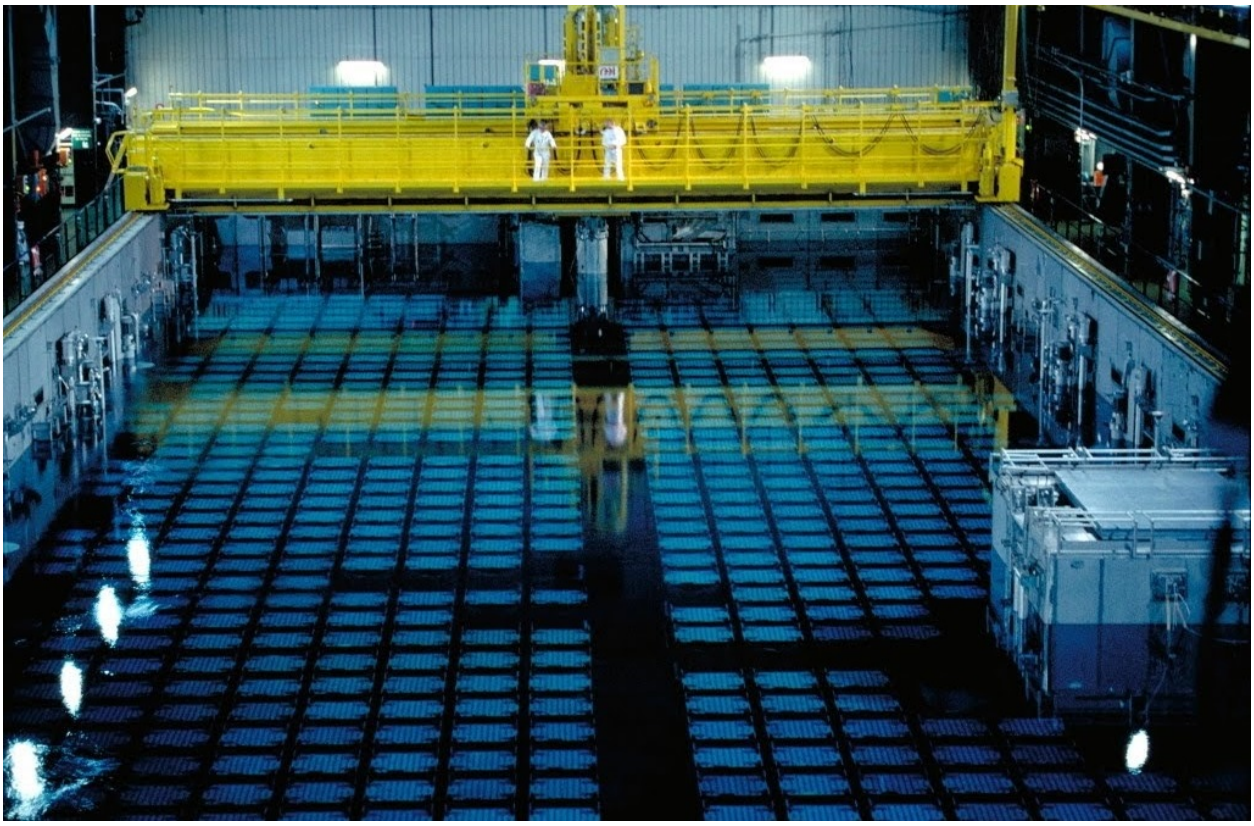

Figure 2: Example of commercial used nuclear fuel storage pool [2]

Within the current American fuel cycle paradigm, the used fuel assemblies remain in the fuel storage pools for 10 to 20 years following their removal from the reactor. It should be noted

that this timeframe is an industry average since the actual period in which fuel assemblies are placed in active cooling is dependent on the current capacity of a utility's fuel storage pool and the availability of additional passive cooling systems. Once the fuel assemblies have cooled sufficiently to be removed from the active cooling system, the fuel assemblies are loaded in dry cask storage systems which passively cool the used fuel via natural convection. Dry cask storage systems are massive structures comprised principally of two components: (1) a thin-walled metallic canister; (2) a thick-walled reinforced-concrete storage module. The cooled fuel assemblies are loaded into the compartmentalized thin-walled canister which is backfilled with an inert gas (generally helium) and sealed. Using a specially designed transfer cask, the loaded canister is transported to the concrete storage module where a hydraulic ram is used to insert the cylinder to its final stored position. An example of a horizontally-oriented dry cask system, specifically Transnuclear's NUHOMS modular storage system, is displayed in Figure 3.

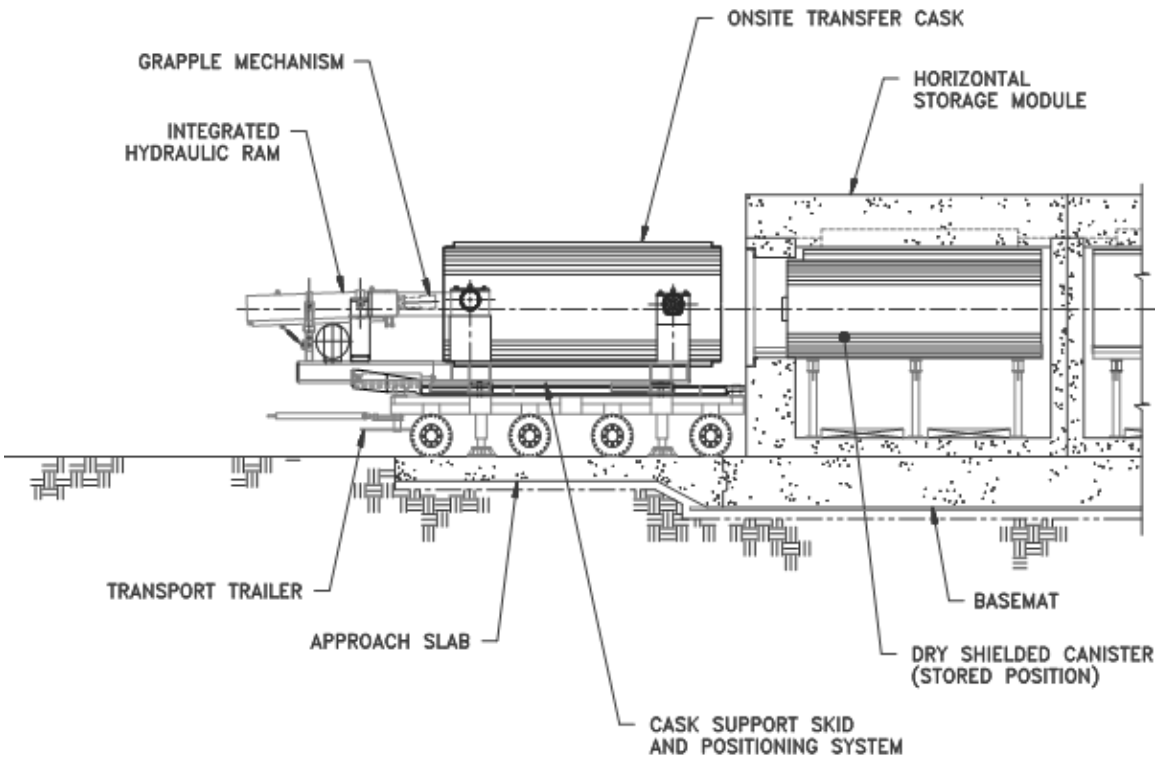

Figure 3: Horizontally-oriented NUHOMS dry cask system [3]

Once the sealed canister, now loaded with used nuclear fuel assemblies, reaches its final, stored position, heat is dissipated from the surface via natural convection. Cool air at ambient conditions enters the vents at the bottom of the storage module and gains thermal energy as it passes over the surface of the canister. Fluid motion through the horizontal storage module is driven by the density gradient between the entering (low temperature) and exiting (high temperature) air. In this configuration, the heat within the fuel assemblies is relinquished to the ambient air and the decay energy is mitigated passively through buoyancy-induced flow.

1.1 ISSUES WITH USED FUEL STORAGE POOLS

Since the construction of the first commercial nuclear power generating facilities, fuel storage pools have been designed under the premise that the storage of used nuclear fuel would only occur temporarily on-site. It was assumed that after a few years of storage at the plant's own fuel storage pool, the assemblies would be transported to a reprocessing facility where the remaining uranium and plutonium isotopes would be recycled for future usage. Throughout the first two decades of nuclear power generation in the United States, used fuel assemblies were accumulated within on-site fuel storage pools where they awaited the finalization of a centralized reprocessing facility. It was at this time, however, that physicists in India constructed and tested a nuclear device comprised of plutonium recovered from used commercial fuel sources. On April 7th, 1977, three years after the successful performance of India's plutonium-based device, the Carter administration responded by halting the licensing of a nearly-completed reprocessing facility in an effort to prevent the acquisition of separated plutonium. At the time, it was believed that by being proactive on this measure, other countries may follow suit before pursuing the development of

their own nuclear arsenal. To combat the large inventories of used nuclear fuel assemblies already produced, as well as those yet to be depleted, Congress established the National Waste Policy Act (NWPA) in 1982, which initiated the development of a long-term nuclear waste repository at Yucca Mountain. Initially set to receive fuel in 1998, the Yucca Mountain repository project has been the subject of countless political and technical delays and it is unknown at this time if the site will ever come to fruition.

In response to the delays in the development of the Yucca Mountain nuclear waste repository, the Nuclear Regulatory Commission (NRC) has allowed for the high-density storage of used nuclear fuel assemblies within on-site fuel pools. These types of storage configurations employ borated dividers between densely-packed fuel elements to prevent criticality between adjacent assemblies. Although this provides an acceptable method for housing used fuel assemblies after their time within the reactor core, high-density fuel pool storage concentrates large inventories of highly-radioactive isotopes, such as cesium-137 (Cs-137) and iodine-131 (I-131), in a centralized location. Furthermore, investigations have analyzed the safety of high-density fuel pool storage and observed the susceptibility of these storage configurations to loss-of-coolant accident (LOCA) scenarios. Many within the industry have called for the reduction of current fuel pool inventories by mandating a maximum permissible time in which fuel assemblies may be placed in wet storage [1]. By accelerating the transfer from active wet storage to passive dry storage conditions, the centralized inventory of highly radioactive isotopes is spread across multiple fortified dry cask systems. Additionally, the passive nature of dry cask storage systems allow for constant heat rejection, even during complete loss of onsite power scenarios analogous to the incident at the Fukushima Daiichi Nuclear Power Plant.

1.2 HIGH-BURNUP USED NUCLEAR FUEL

In an effort to maximize fuel utilization and reduce the amount of fuel assemblies that ultimately need to be stored, recycled, or disposed, commercial nuclear energy generators have shifted towards operating fuel to high, or extended burnups. By increasing the initial enrichment of fissile materials, utilities are able to operate longer at full-power conditions, reduce their fuel cycle costs, and decrease the radiation doses received by plant workers. This industry-wide movement is displayed graphically in Figure 4, which validates this trend by analyzing the current and future usage of fuel assemblies at the 45 GWd / MTU burnup level. Figure 4's graphic representation of the past, present, and future nuclear fuel burnup trend clearly delineates the shift towards higher-burnup fuel and phase-out of fuel at lower burnup levels.

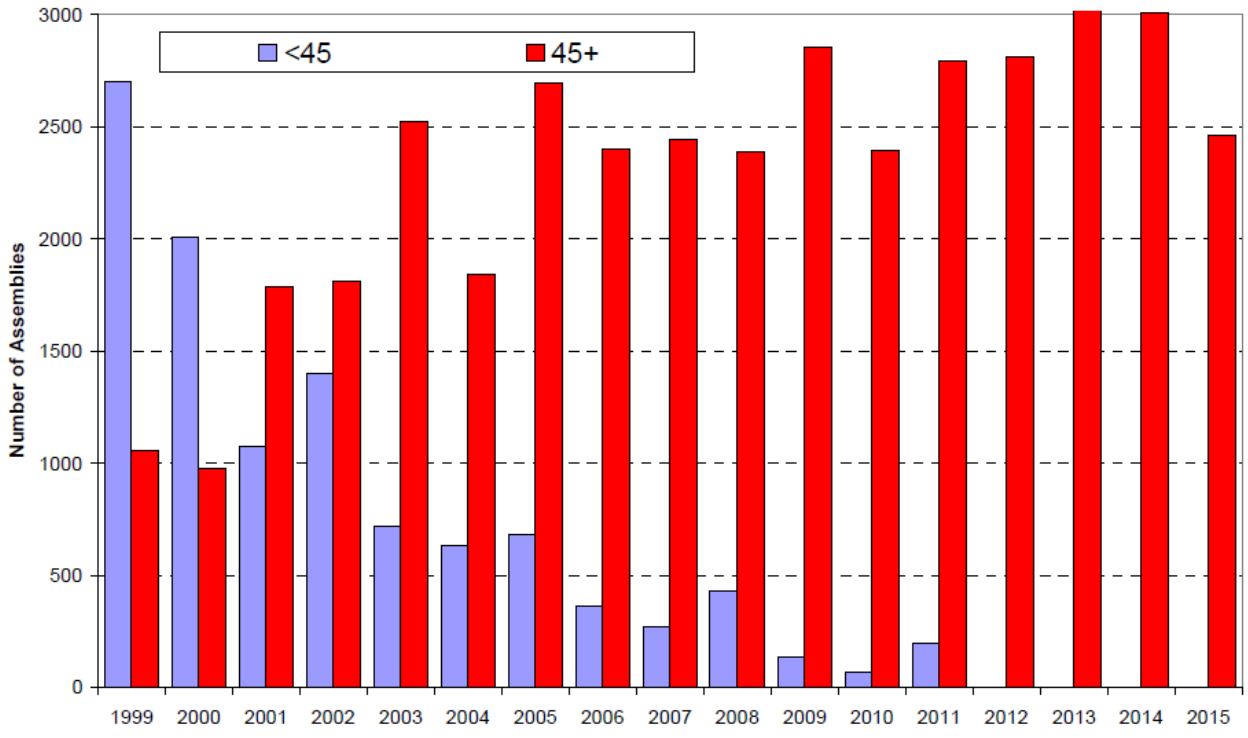

Figure 4: Projected number of discharged PWR fuel assemblies with burnup levels above and below 45 GWd / MTU [4]

Although utilizing fuel to higher burnups presents many benefits from a sustainable fuel cycle perspective, the decay heat present at higher burnups offers cause for concern during used fuel storage. Previously alluded to in Figure 1, the decay heat energy content for high-burnup used nuclear fuel can be significantly greater than that of their lower-burnup counterparts. This decreased energy content is a direct result of the increased fuel utilization; since more fissile material is being fissioned, more radioactive fission products are being generated, thus leading to an increase in the high energy beta and gamma decays. Perhaps more interesting than the overall time-dependent nature of these higher-burnup assemblies is their energy content relative to standard nuclear fuel. A representation of the time-dependent decay energy profile for high-burnup used nuclear fuel relative to that of a standard burnup level is offered in Figure 5.

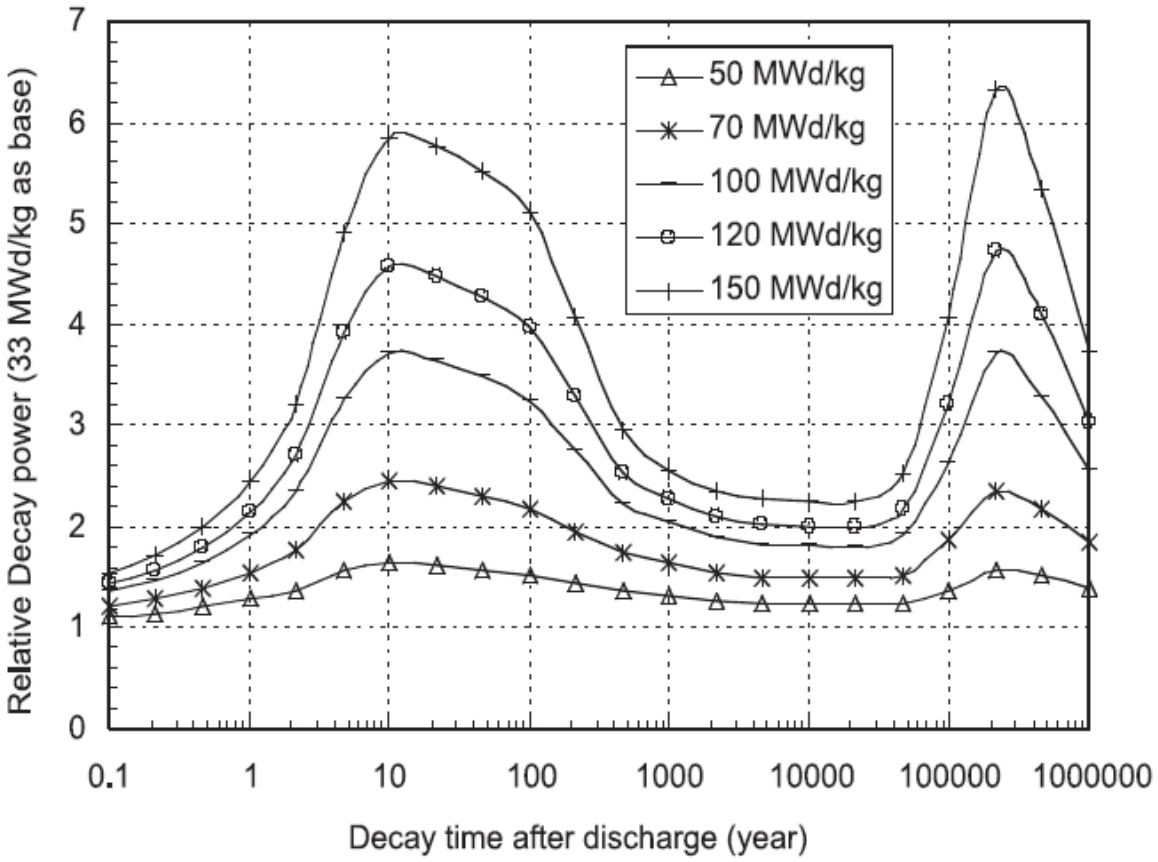

Figure 5: Relative decay power (33 MWd / kg U Base) [5]

Analyzing the shapes of the relative decay power distribution in Figure 5 reveals a local maximum around 10 years after discharge from the reactor, which coincides with the timeframe associated with transfer from wet to dry storage conditions. Using the projected pressurized water reactor (PWR) fuel assembly trend data from Figure 4, fuel removed from current and future reactors would have approximately 160% more thermal energy than fuel currently being loaded into dry cask storage systems. Likewise, if the current fuel burnup trend continues, dry cask storage systems may soon face fuel assemblies with decay energy levels anywhere between 175 to 250% of their present-day counterparts. The difference in energy content between present and future used nuclear fuel presents itself as a significant challenge for any potential accelerated transfer initiative. To combat these higher decay energy levels, dry cask designs, both current and future, must have an increased emphasis on maximizing the thermal capacity of their systems.

1.3 OBJECTIVES

The principal goal of this investigation is to develop a fundamental understanding of the physics associated with the buoyancy-induced flow around dry casks in an effort to improve the heat rejection capability of the overall system. Based on the geometry of horizontally-oriented dry cask systems, the natural convection problem is very analogous to that of a heated horizontal cylinder confined between two vertical, adiabatic walls. In such geometrical configurations, it has been shown that the distance between the cylinder and the confining wall can have an impact on the natural convection flow itself and heat rejection capacity of the fluid. In order to evaluate both the natural convection phenomenon around the heated dry cask canister and the effect wall distance

plays on the heat rejection capability, the problem geometry is reduced to a two-dimensional cross-section of the aforementioned scenario.

To evaluate the coupled heat and mass transfer within the proposed problem geometry, computational fluid dynamics (CFD) models are constructed and analyzed. Within each simulation, the distance between the confining walls relative to the diameter of the internal cylinder serves as an independent variable. Additionally, the magnitude of the heat rejection in natural convection flow regimes is dependent on the buoyancy of the fluid, a function of both the geometry and thermal energy of the confined cylinder. By varying the degree of the fluid's buoyancy and the distance between the confining walls, the impact of each factor on the heat rejection from the cylinder can be quantified numerically. As only a two-dimensional cross-section is considered in this investigation, the variation in the buoyancy of the fluid is limited such that the fluid remains in the laminar flow region. The subsequent simulations will serve as a preliminary tool for dry cask systems designers as they attempt to analyze what factors improve the thermal capacity of their projects.

1.4 THESIS ORGANIZATION

This thesis reviews the research of previous investigators who have analyzed this particular problem and outlines and summarizes the findings of the current CFD simulations. A review of the current and past literature on the natural convection from a confined horizontal cylinder is present in Chapter 2.0 . Chapter 3.0 delineates the methodology and theory behind the CFD simulations and defines the key parameters, both independent and dependent, that were analyzed over the course of this investigation. Chapters 4.0 and 5.0 house the bulk of the results from the

current investigation while Chapter 6.0 demonstrates the value of these findings to dry cask designers. Additionally, Chapter 6.0 proposes future CFD simulations that could assist in the development of higher thermal capacity dry cask systems.

2.0 LITERATURE REVIEW

Although the problem of natural convection from a heated horizontal cylinder has been the subject of numerous investigations, the interactive flow due to a heated horizontal cylinder in a vertical channel has been less comprehensively studied. The purpose of this chapter is to provide a literature review of natural convection investigations involving heated horizontal cylinders, both unconfined and confined. Segregated into two main sections, this chapter will first review studies associated with natural convection from a single, unconfined heated horizontal cylinder. Within the second section, investigations which analyzed the interactive effect of vertical confining walls on the buoyancy-induced flow will be summarized.

2.1 FREE CYLINDER

Investigations on the topic of the buoyancy-induced flow around a heated horizontal cylinder are generally categorized into one of three distinct groups: (1) theoretical; (2) experimental; (3) numerical. Due to the formation of a wake at the top of the cylinder, theoretical solutions for laminar natural convection around a horizontal cylinder are often far less accurate than those produced for flat plates [6]. For the sake of brevity, early theoretical works employing boundary-layer and series solutions are omitted from this literature review in favor for a more detailed discussion on major experimental and numerical methodologies.

Early experimental efforts focused on developing correlations between the effective rate of heat transfer from the cylinder surface and the buoyancy and material properties of the

surrounding fluid. In an effort to simplify the correlating relationships, initial investigators employed two dimensionless quantities, the Nusselt (Nu) and Rayleigh (Ra) number, to quantify the two aforementioned problem characteristics. Each of these dimensionless parameters, as well as others introduced throughout this literature review, will be discussed in more detail in the ensuing background section of this thesis.

Using previously established experimental data from horizontal pipes, McAdams [7] recommended one of the first empirical correlations to determine heat transfer at the surface of an isothermal cylinder:

$$\mathrm{Nu}_\infty = 0.53\mathrm{Ra}^{0.25} \tag{1}$$

where Nu_∞ refers specifically to the average Nusselt number at the surface of an unconfined cylinder. Based on the available experimental data, McAdams indicated this correlation provided an acceptable fit provided that $10^3 < \mathrm{Ra} < 10^9$. Morgan [8] expanded on the work of McAdams to develop the following piecewise expression relating the Nusselt and Rayleigh numbers:

$$\mathrm{Nu}_\infty = C\mathrm{Ra}^m \tag{2}$$

where the correlating parameters C and m are determined from the Rayleigh number of the flow around the cylinder. Table 1 details the applicable correlating parameters for Equation (2) for a series of finite Rayleigh number ranges between 10^{-4} and 10^{12}. Morgan claimed that the proposed correlation in Equation (2) has a maximum uncertainty of ± 5% over the whole given range of Rayleigh numbers, except in the transition regions at values of 10^{-2}, 10^2, 10^4, and 10^7 since the abrupt changes in the gradient of the mathematical expressions in these regions is not reflective of the actual physics.

Table 1: Morgan correlation parameters [8]

Range of Ra	C	m
10^{-4} to 10^{-2}	0.675	0.058
10^{-2} to 10^{2}	1.020	0.148
10^{2} to 10^{4}	0.850	0.188
10^{4} to 10^{7}	0.480	0.250
10^{7} to 10^{12}	0.125	0.333

Churchill and Chu [9] combined boundary-layer theory formulations with experimental data to generate a representative expression for the natural convection heat transfer from an unconfined horizontal cylinder. Unlike the previous formulations of McAdams and Morgan, Churchill and Chu concluded that the rate of heat transfer is also related to the Prandtl (Pr) number of the fluid. Within the laminar regime, they proposed that the average Nusselt number at the surface of a cylinder could be evaluated via:

$$\mathrm{Nu}_{\infty} = 0.36 + 0.518\left(\frac{\mathrm{Ra}}{\left[1+\left(\frac{0.559}{\mathrm{Pr}}\right)^{9/16}\right]^{16/9}}\right)^{1/4} \tag{3}$$

which was demonstrated to provide a good representation of available experimental data for all Prandtl numbers and $10^{-6} < \mathrm{Ra} < 10^{9}$.

Fand et. al. [10] empirically examined the rate of heat transfer via natural convection from horizontal cylinders to air, water, and silicone oils in the experimental rangers of $2.5 \times 10^{2} \leq \mathrm{Ra} \leq 1.8 \times 10^{7}$. From their extensive collection of experimental heat transfer coefficient data, a comprehensive correlation was offered to account for both the buoyancy and material properties of the fluid:

$$\mathrm{Nu}_{\infty} = 0.474\mathrm{Ra}^{0.25}\mathrm{Pr}^{0.047} \tag{4}$$

Using the correlations of Morgan and Churchill and Chu as points of comparison, the investigators theorized that the subtle differences between empirical correlations and experimental data could be attributed to a viscous dissipation heat transfer mechanism that was neglected in every relationship. From this hypothesis, Fand and Brucker [11] proposed including an additional dimensionless parameter, the Gebhart number, to account for the viscous dissipation of thermal energy. Using experimental data ranging from $0.7 < \mathrm{Pr} < 4 \times 10^4$ and $10^{-8} < \mathrm{Ra} < 10^8$, they suggested that the Nusselt number at the surface of an unconfined cylinder could be evaluated by:

$$\mathrm{Nu}_\infty = \mathrm{Pr}^{0.0432}\mathrm{Ra}^{0.25} + 0.503\mathrm{Pr}^{0.0334}\mathrm{Ra}^{0.0816} + \frac{0.958\mathrm{Ge}^{0.122}}{\mathrm{Pr}^{0.0600}\mathrm{Ra}^{0.0511}} \tag{5}$$

where the Gebhart number can be determined from the fluid material properties via Equation (6).

$$\mathrm{Ge} = \frac{g\beta D}{c_p} \tag{6}$$

The characteristic correlation presented in Equation (5) proved to be more representative of the natural convection phenomenon than the simpler expressions presented in [7-10]. Fand and Brucker concluded that viscous dissipation may not be neglected in all cases of natural convection from horizontal cylinders, and further, that the inclusion of a viscous dissipation term may lead to a more accurate representation of the buoyancy-induced flow.

Analogous to their empirical counterparts, numerical investigators sought to evaluate the buoyancy-induced flow to quantify the heat transfer phenomenon at the surface of the unconfined horizontal cylinder. Kuehn and Goldstein [12] employed a finite-difference method to evaluate the two-dimensional vorticity-stream function formulation of the Navier-Stokes equations. Within their investigation, Kuehn and Goldstein obtained numerical solutions for the local and average Nusselt number at Pr = 0.70 over the range $10^0 < \mathrm{Ra} < 10^7$. Additionally, angular and radial velocities and temperature profiles were computed at Pr = 0.7 and $\mathrm{Ra} = 10^5$ and compared to

boundary-layer analyses. At Ra = 10^4, the boundary layer thickness at the horizontal centerline of the cylinder was approximately equal to the cylinder radius and they observed a decrease in layer size at higher Rayleigh numbers. Within the radial and velocity distributions, they observed a flow separation around 150° from the bottom of the cylinder. Beyond that point, the turning of the flow to form a plume significantly altered the temperature distribution and the thermal boundary layer thickened.

Farouk and Güçeri [13] validated the work of Kuehn and Goldstein using a slightly different finite-difference methodology. They too evaluated the two-dimensional vorticity-stream function formulation of the Navier-Stokes equations within their curvilinear numerically-generated computational grids. Within Pr = 0.7 and $10^3 < Ra < 10^7$, Farouk and Güçeri obtained mean Nusselt numbers that were nearly identical to those tabulated by Kuehn and Goldstein. Likewise, tangential velocities at Pr = 0.7 and Ra = 10^5 corresponded to the values determined in [12] and the same flow separation phenomenon was observed.

2.2 CONFINED CYLINDER

Unlike the natural convection around an unconfined horizontal cylinder, there has not been a comprehensive investigation into the buoyancy-induced flow around a heated cylinder confined between two adiabatic walls. Analogous to the results produced for its unconfined counterparts, the natural convection around a confined cylinder can be quantified by evaluating the relative heat transfer rate from the cylinder surface as a function of the system Rayleigh number and magnitude of confinement. Several investigators have analyzed this phenomenon in an effort to determine the optimal distance between the confining walls such that the rate of heat transfer is maximized.

Within the first systematic solution to this scenario, Marsters [14] employed both experimental and analytical methods over a vast range of Rayleigh numbers. Despite the level of detail in his initial experimental studies, Marsters did not observe an optimal wall distance around the heated cylinder.

Farouk and Güçeri [15] expanded upon their unconfined heated cylinder investigation and analyzed natural and mixed convection heat transfer on a confined horizontal cylinder. During their natural convection analyses, Farouk and Güçeri implemented their two-dimensional vorticity-stream function formulation of the Navier-Stokes equations for three different Rayleigh numbers: 10^3, 10^4, and 10^5. By employing the ratio of the distance between the confining walls relative to the diameter of the cylinder as an independent variable, the investigators were able to evaluate the effect confinement plays on the rate of natural convection heat transfer. Over the three analyzed confinement ratios, a mixed effect on the surface average Nusselt number was observed such that no discernable trend was detected. Likewise, the investigators did not observe any behavior that would suggest the existence of an optimal wall distance such that the natural convection heat rejection is maximized.

Sadeghipour and Kazemzadeh [16] employed a transient finite-element methodology to investigate the natural convection heat transfer from a confined horizontal cylinder. They evaluated one Rayleigh number ($Ra = 10^3$) over a wide range of confinement ratios and analyzed the effect on the mean Nusselt number at the surface of the cylinder. Within their range of analysis, Sadeghipour and Kazemzadeh detected a maxima in the numerically determined mean Nusselt numbers at a confinement ratio of approximately 2.5.

Sadeghipour and Yazdan [17] expanded upon the work of [14] and [16] with a theoretical, experimental, and numerical investigation of laminar natural convection from a horizontal cylinder

confined between two vertical walls. In their investigation, Sadeghipour and Yazdan employed an integral method akin to the work of Marsters to develop an analytical solution for the heat transfer behavior of the confined cylinder at the two extreme confinement ratios (C): (1) $C \rightarrow 1$; (2) $C \rightarrow \infty$. Based on the derived analytical solutions at these boundary conditions, they claimed that an optimal wall confinement exists for each unique Rayleigh number. This claim is supported by the empirical data collected over four distinct Rayleigh numbers (649.8, 767.7, 842.7, and 910.0) and at six different confinement ratios (1.5, 3.0, 6.0, 8.0, 12.0, and ∞). At each of the analyzed Rayleigh numbers, an optimal confinement ratio is observed in the collected empirical data.

2.3 RESEARCH MOTIVATION

Previous work at the University of Pittsburgh [18] focused on novel methods by which to remove thermal energy from sealed dry cask storage systems. Several full-sized computational models of commercially-available dry cask storage systems have been constructed and evaluated for their thermal performance over a range of appropriate thermal decay energy loads. However, this proved to be problematic for a number of reasons. First, the high amount of turbulence generated by the size and thermal energy content of the canister precluded two-dimensional analysis. Furthermore, numerical issues resulting from the transient nature of highly-turbulent flow caused stability issues for a majority of the computational models.

The goal of this thesis is to focus on evaluating the fundamental physics associated with the buoyancy-induced flow around a confined heated horizontal cylinder. As previously stated, several researchers have investigated this particular scenario, but no true fully-comprehensive solution to the laminar natural convection heat transfer problem has been established. It is the

ultimate goal of this investigation to capture the effect of wall confinement on the rate of heat transfer from the surface of isothermal and isoflux cylinders. Although the Rayleigh numbers for typical dry cask scenarios suggest a high level of turbulence, the fundamental configuration explored in this thesis provides a critical first step in ultimately characterizing the buoyancy-driven convection and exploiting this to the maximum extent possible.

3.0 PROBLEM DESCRIPTION

3.1 PROBLEM GEOMETRY

In order to evaluate the buoyancy-induced flow regime about a confined, heated horizontal cylinder, a two-dimensional computational model is created and analyzed using the FLUENT flow modeling simulation software. A fundamental depiction of the problem geometry, complete with labels of pertinent geometric variables, is displayed in Figure 6.

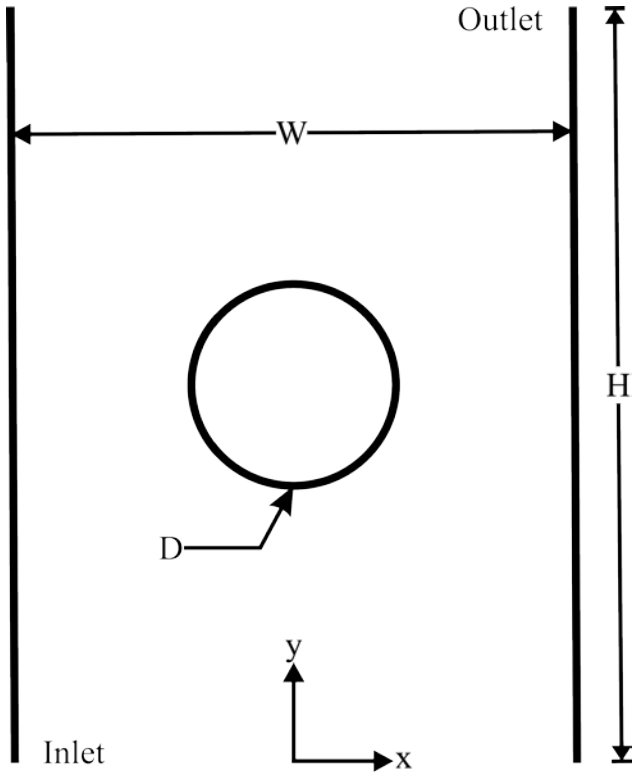

Figure 6: Schematic of problem geometry

For this particular configuration, two principal independent variables are utilized to characterize the geometry and flow within the computational domain: confinement ratio and

Rayleigh number, respectively. The confinement ratio (C), which is a ratio of the distance between the vertical walls to the diameter of the confined cylinder, can be defined symbolically as:

$$C = \frac{W}{D} \tag{7}$$

such that the condition $C > 1$ must be maintained.

For the definition of flow characteristics in natural convection problems, the product of the Grashof and Prandtl numbers, or Rayleigh number, is the most commonly used parameter. For the formulation of natural convection around a heated horizontally-oriented cylinder, the average Grashof number is defined as:

$$\mathrm{Gr_D} = \frac{g_c \rho^2 \beta D^3}{\mu^2}(T_s - T_\infty) = \frac{g_c \beta D^3}{\nu^2}(T_s - T_\infty) \tag{8}$$

where g_c is the gravitational constant, ρ is the fluid density, β is the compressibility of the fluid, T_s is the temperature at the surface of the cylinder, T_∞ is the bulk temperature of the quiescent fluid, D is the diameter of the cylinder, μ is the molecular viscosity of the fluid, and ν is the kinematic viscosity of the fluid. Conceptually, the Grashof number can be thought of as a ratio of the buoyant force relative to the viscous force acting on the fluid. Likewise, the Prandtl number, which is a ratio of the fluid's ability to diffuse momentum relative to its ability to diffuse thermal energy, is defined as:

$$\mathrm{Pr} = \frac{c_p \mu}{k} = \frac{\nu}{\alpha} \tag{9}$$

where c_p is the specific heat of the fluid, k is the thermal conductivity of the fluid, and α is the thermal diffusivity of the fluid. For the free convection around a heated horizontal cylinder, the Rayleigh number can be determined from the product of the Grashof and Prandtl numbers displayed in Equations (8) and (9), respectively.

$$\mathrm{Ra_D} = \mathrm{Gr_D Pr} = \frac{g_c \beta D^3}{\alpha \nu} (T_s - T_\infty) \tag{10}$$

As the chief purpose of this investigatory work is to analyze the impact confinement ratio plays on the convective heat transport from the surface of dry cask canisters, it is also prudent to analyze this particular geometric configuration without assuming a constant temperature at the surface of the cylinder. Since dry cask systems are generally uniformly loaded with equal power used nuclear fuel assemblies, the surface of the mock two-dimensional cylinder can also be treated with a constant heat flux condition. With such a surface treatment, the Grashof and Rayleigh numbers need to be redefined based on the heat flux exiting the cylinder in the radial direction. As proposed by previous researchers [9], the following first-order approximation can be utilized to relate the heat flux to a temperature difference at the cylinder surface:

$$(T_s - T_\infty) \approx \frac{q'' D}{k} \tag{11}$$

where q'' is the heat flux exiting the cylinder in the direction normal to the surface.

Using the approximation in Equation (11) in conjunction with the definition of the standard Grashof number in Equation (8) allows for the characterization of the modified Grashof number:

$$\mathrm{Gr_D^*} = \frac{g_c \rho^2 \beta D^4}{k \mu^2} q'' = \frac{g_c \beta D^4}{k \nu^2} q'' \tag{12}$$

which is dependent on the heat flux at the surface of the cylinder. Likewise, an analogous transformation to the standard definition of the Rayleigh number allows for the development of a heat flux-dependent modified Rayleigh number:

$$\mathrm{Ra_D^*} = \mathrm{Gr_D^* Pr} = \frac{g_c \beta D^4}{\alpha \nu k} q'' \tag{13}$$

3.2 MODELING TECHNIQUE

Using the relationships for the confinement ratio and appropriate definition of the Rayleigh number, the parameters of each numerical simulation can be evaluated. For the purposes of this investigation, the diameter of the confined horizontal cylinder is fixed across all of the numerical simulations. Thus, the confinement ratio is varied by widening or constricting the width of the confining walls adjacent to the heated cylinder. Additionally, the height of the vertical channel, H, is fixed such that the relationship:

$$H = 30D \tag{14}$$

is satisfied.

Analogous to the treatment of the system's confinement ratio, a modeling simplification is applied to the definition of the Rayleigh number to simplify the process of simulating multiple independent parameter combinations. In each of the isothermal numerical simulations, the temperature of the cylinder surface is assumed to be one degree higher than that of the quiescent air medium. By treating the surface temperature in this manner, the fluid properties are able to be treated as constants at the film temperature of the system:

$$T_f = \frac{T_s - T_\infty}{2} \tag{15}$$

To account for this simplification within the definition of the flow characteristics in each simulation, the effective gravitational constant in each numerical model is calculated from the desired Rayleigh number. For simulations with a constant temperature along the length of the cylinder's surface, the effective gravitational constant used in each model is evaluated via:

$$g_{eff} = \frac{\alpha\nu}{\beta D^3}\,\mathrm{Ra_D} \tag{16}$$

For cases in which the surface of the cylinder is treated with a constant heat flux condition, the identical simplification allows for the approximation of the scalar heat flux:

$$q'' \approx \frac{k}{D} \tag{17}$$

By using this formulation of the scalar heat flux, the effective gravitational constant for models employing constant heat fluxes at the cylinder surface is equivalent to isothermal scenario:

$$g_{eff}^{*} = g_{eff} = \frac{\alpha \nu k}{q'' \beta D^4} \mathrm{Ra}_{\mathrm{D}}^{*} = \frac{\alpha \nu}{\beta D^3} \mathrm{Ra}_{\mathrm{D}} \tag{18}$$

3.3 GOVERNING EQUATIONS

The formulation of buoyancy-induced problems follows the same basic conservation principles that govern general fluid motion, namely the conservation of mass, momentum, and energy. Unlike forced flow studies in which fluid properties are assumed to be constant throughout the domain of interest or exist as point functions which can be evaluated within the respective conservation relationship, natural convection scenarios require at least one fluid parameter, density, to vary within the domain of interest. Starting from the most conservative form of the aforementioned mass and momentum conservation equations, the buoyancy-induced flows about a horizontal cylinder can be analyzed via:

$$\frac{d\rho}{dt} + \nabla \cdot (\rho \cdot \vec{v}) = 0 \tag{19}$$

$$\frac{d}{dt}(\rho \cdot \vec{v}) + \nabla \cdot (\rho \vec{v} \vec{v}) = -\nabla P + \nabla \cdot \vec{\vec{\tau}} + \rho \vec{g} \tag{20}$$

Based on the problem geometry considered over the course of this investigation, the mass and momentum conservation equations can be simplified to only consider fluid movement in the

x- and y-directions. Additionally, since these numerical simulations are intended to run at low and moderate Rayleigh numbers, the time-dependent component of the Navier-Stokes equations can be neglected to obtain only the steady-state flow characteristics. The stress tensor in the momentum expression, $\vec{\vec{\tau}}$, can be expanded to:

$$\vec{\vec{\tau}} = \mu\left[(\nabla \cdot \vec{v} + \nabla \cdot \vec{v}^T) - \frac{2}{3}\nabla \cdot \vec{v}I\right] \tag{21}$$

where I is the identity matrix and the second term on the right-side of the expression accounts for the dilation of the volume under evaluation. As these numerical simulations intend to analyze natural convection due to density variations of a gas, the volume dilation term can be neglected. Due to the close proximity of the temperature limits imposed in the problem specification, the molecular viscosity of the fluid is assumed to be constant at all points in the domain. By making these simplifications and expansions, Equations (19) and (20) can be rewritten as:

$$\nabla \cdot (\rho \cdot \vec{v}) = 0 \tag{22}$$

$$\nabla \cdot (\rho \vec{v}\vec{v}) = -\nabla P + \mu(\nabla^2 \cdot \vec{v}) + \rho\vec{g} \tag{23}$$

As the principal concern of these simulations is to evaluate the buoyancy-induced flow regime about a heated surface, the temperature-induced variation of the fluid density plays a crucial role in the overall flow analysis. To simplify the evaluation of the fluid density at all points within the domain, the Oberbeck-Boussinesq approximation is employed to linearize the temperature dependency of density in the buoyancy force. From this approximation, the buoyancy force is redefined as:

$$\rho\vec{g} = \vec{g}\left[\rho_{ref} - \rho_{ref}\beta\left(T - T_f\right)\right] = \rho_{ref}\vec{g}\left[1 - \beta\left(T - T_f\right)\right] \tag{24}$$

where ρ_{ref} is the fluid density at the film temperature T_f and β is the compressibility of the fluid evaluated via:

$$\beta = -\frac{1}{V}\frac{\partial V}{\partial P} \tag{25}$$

Since the temperature difference between the surface of the cylinder and ambient air is only one degree, the compressibility of the fluid can be treated as a constant. Additionally, since air behaves as an ideal gas at nominal atmospheric pressures and temperatures, the compressibility of the air can be determined via:

$$\beta = \frac{1}{T_f} \tag{26}$$

Inherent in the utilization of the Oberbeck-Boussinesq approximation is that any variations in the fluid density are only considered in the buoyancy term. Therefore, the density in each of the other terms in the mass and momentum expressions can be removed from their respective gradients and treated as constants. Furthermore, the variations in density are assumed to only occur when they influence the bulk movement of the fluid, meaning that the newly defined Oberbeck-Boussinesq form of the buoyancy force is only present in the y-direction momentum expression. Making the necessary simplifications to the mass and momentum equations present in Equations (22) and (23) allows for the development of the final forms:

$$\nabla \cdot \vec{v} = 0 \tag{27}$$

$$\vec{v} \cdot (\nabla \cdot \vec{v}) + \vec{v} \cdot (\nabla \cdot \vec{v}) = -\frac{1}{\rho_{ref}} \nabla P + \nu_{ref} (\nabla^2 \cdot \vec{v}) + \vec{g}\left[1 - \beta\left(T - T_f\right)\right] \tag{28}$$

Equivalently, Equation (27) can be inserted into Equation (28) and the resulting formulation of the Navier-Stokes equation can be split into separate x and y-direction expressions:

X-Direction:

$$v_x \frac{\partial v_x}{\partial x} + v_y \frac{\partial v_x}{\partial y} = \frac{1}{\rho_{ref}}\left(-\frac{\partial P}{\partial x}\right) + \nu_{ref}\left(\frac{\partial^2 v_x}{\partial x^2} + \frac{\partial^2 v_x}{\partial y^2}\right) \tag{29}$$

Y-Direction:

$$v_x \frac{\partial v_y}{\partial x} + v_y \frac{\partial v_y}{\partial y} = \frac{1}{\rho_{ref}}\left(-\frac{\partial P}{\partial y}\right) + \nu_{ref}\left(\frac{\partial^2 v_y}{\partial x^2} + \frac{\partial^2 v_y}{\partial y^2}\right) + g_{eff}\left[1 - \beta\left(T - T_f\right)\right] \quad (30)$$

In order to evaluate the temperature at all points within the computational domain, a separate conservation of energy relationship needs to be developed and analyzed simultaneously to the two momentum expressions. From its most conservative incarnation, the conservation of energy relationship can be expressed via:

$$\frac{\partial}{\partial t}(\rho h) + \nabla \cdot (\rho h \vec{v}) = -\nabla \cdot q'' + q''' + \frac{\partial P}{\partial t} + \nabla \cdot (P\vec{v}) + \Phi \quad (31)$$

where h is the enthalpy of the fluid, q''' is the volumetric heat generation rate, and the final term on the right side of the expression, Φ, accounts for the viscous dissipation of energy. Following the application of the continuity equation and the removal of the temporal derivatives, Equation (31) can be simplified to:

$$\rho\vec{v} \cdot \nabla h + h\vec{v} \cdot \nabla \rho = -\nabla \cdot q'' + q''' + \nabla \cdot (P\vec{v}) + \Phi \quad (32)$$

The heat flux in Equation (32) is the sum of the individual heat fluxes resulting from conduction and radiation heat transfer modes. As the temperature of the fluid is air and is bounded between two low temperatures (299.5 and 300.5 K), the impact of radiation heat transfer is not anticipated to be significant and can be safely neglected. Therefore, the gradient of the conduction heat flux can be transformed via Fourier's law of conduction to:

$$-\nabla \cdot q_c'' = \nabla \cdot (k \nabla T) \quad (33)$$

Additionally, since the principal fluid of interest is air, the volumetric heat generation term can also be set to zero.

Analogous to the treatment of the fluid properties in the conservation of mass and momentum equations, each fluid property present in the conservation of energy relationship is

assumed to be constant throughout the problem geometry. This simplification reduces Equation (32) to:

$$\rho_{ref}\vec{v}\cdot\nabla h = k_{ref}\nabla^2 T + \nabla\cdot(P\vec{v}) + \mu_{ref}\Phi \tag{34}$$

where the two-dimensional viscous dissipation function can be expressed as:

$$\Phi = 2\left(\frac{\partial v_x}{\partial x}\right)^2 + 2\left(\frac{\partial v_y}{\partial y}\right)^2 + \left(\frac{\partial v_x}{\partial y} + \frac{\partial v_y}{\partial v_x}\right)^2 \tag{35}$$

One final thermodynamic transformation is necessary to convert the enthalpy formulation in Equation (34) to a more conventional temperature-based relationship. From the definition of enthalpy and entropy, the differential enthalpy can be written as:

$$dh = c_p dT + (1-\beta T)\frac{dP}{\rho} \tag{36}$$

Since the compressibility of the air was treated as an ideal gas during the derivation of the momentum conservation equation, the same assumption can be applied to the derivation of the conservation of energy. Thus, the second term on the right-side of Equation (36) is reduced to zero, leaving only the product of the specific heat and differential temperature. Therefore, the final form of the energy conservation equation can be expressed via:

$$\rho_{ref}c_{p_{ref}}\vec{v}\cdot\nabla T = k_{ref}\nabla^2 T + \nabla\cdot(P\vec{v}) + \mu_{ref}\Phi \tag{37}$$

or in two-dimensional Cartesian coordinates:

$$\begin{aligned}\left[\rho_{ref}c_{p_{ref}}\left(\frac{\partial T}{\partial x}+\frac{\partial T}{\partial y}\right)\right]\vec{v} \\ = k_{ref}\left(\frac{\partial^2 T}{\partial x^2}+\frac{\partial^2 T}{\partial y^2}\right) + P\left(\frac{\partial v_x}{\partial x}+\frac{\partial v_y}{\partial y}\right) + \vec{v}\left(\frac{\partial P}{\partial x}+\frac{\partial P}{\partial y}\right) + \mu_{ref}\Phi\end{aligned} \tag{38}$$

Using Equation (38) in conjunction with the x- and y-direction momentum relationships from Equations (29) and (30) allows for the determination of the laminar natural convection air flow about the horizontal circular cylinder.

3.4 BOUNDARY CONDITIONS

3.4.1 Cylinder Surface

To bound the momentum expression from Equations (29) and (30) at the surface of the confined cylinder, a no-slip velocity condition is employed. This specific Dirichlet boundary condition, which specifies that the fluid velocity at the surface of the solid cylinder must be zero in all directions, can be expressed symbolically via:

$$v_x = v_y = 0 \tag{39}$$

For the treatment of the energy conservation equation at the surface of the cylinder, the boundary condition applied to the numerical model is dependent on the type of problem being analyzed. Within the isothermal cylinder models, a Dirichlet boundary condition is supplied to impose a constant temperature along the surface of the cylinder:

$$T = T_s \tag{40}$$

where T_s is specified as 300.5 K within each isothermal model. In the alternative formulation, in which the heat flux is assumed to be constant, a Neumann boundary condition is imposed at all computational nodes along the cylinder:

$$\frac{\partial T}{\partial n} = -\frac{q''}{k_{ref}} \tag{41}$$

where n refers to the direction normal to the surface and q'' is the heat flux approximated via Equation (17).

3.4.2 Symmetry Plane

In an effort to reduce the computational resources required to evaluate each numerical model created throughout this investigation, a symmetry condition is applied to the vertical centerline of the problem geometry in Figure 6. By specifying a symmetry plane along the length of the channel, the amount of computational cells required to evaluate each problem is effectively cut in half. Mathematically, the momentum and energy equations can be bounded along the symmetry plane by applying zero-gradient conditions normal to the surface of the boundary for the three independent simulation variables: (1) x-velocity; (2) y-velocity; (3) and temperature.

$$\frac{\partial v_x}{\partial n} = \frac{\partial v_y}{\partial n} = \frac{\partial T}{\partial n} = 0 \tag{42}$$

3.4.3 Confining Wall

Analogous to the treatment of the cylinder surface, the confining wall is treated with a no-slip velocity condition which specifies zero velocities in the x- and y-directions. For the treatment of the energy conservation relationship, the confining wall is assumed to be adiabatic, signifying a zero temperature gradient normal to the partition surface.

$$\frac{\partial T}{\partial n} = 0 \tag{43}$$

3.4.4 Air Inlet / Outlet

Unlike conventional numerical heat and mass transfer simulations where the fluid velocity is explicitly defined at the inlet, the nature of natural convection problems prevents the definition of

the velocity at open boundaries a priori. To effectively model the air motion through the vertical channel, vent conditions are applied at the inlet and outlet locations defined in Figure 6. These vent boundary conditions, which specify a zero pressure differential normal to the open surface, can be expressed symbolically via:

$$\frac{\partial P}{\partial n} = 0 \tag{44}$$

At each of the open surfaces in the two-dimensional cross-section, the total pressure, or sum of the static pressure, dynamic pressure, and gravitational head, is calculated to evaluate the fluid motion through the interfaces:

$$p_0 = p + q + \rho g_{eff} z \tag{45}$$

where p represents the static pressure, q represents the dynamic pressure evaluated via Equation (46), and z represents the local height in the channel relative to the y-position of the inlet.

$$q = \frac{1}{2}\rho v^2 \tag{46}$$

Used in conjunction with the vent boundary condition, the calculated total pressure is used to evaluate the mass flow rate of fluid through the domain during each numerical iteration. Air external to the vertical channel is specified at ambient conditions (299.5 K and 101 kPa) and is assumed to act as an infinite reservoir from which air can be drawn into the domain.

3.5 SOLVER SETTINGS

Within each FLUENT CFD model, the SIMPLE algorithm is employed to couple the inlet and outlet pressure boundary conditions to the velocities at those positions. First presented by Patankar in the early 1970s [19], this solver approximates the velocity by solving the momentum equations

with an initial pressure gradient. As the solution iterates, a new pressure field is determined and the mass fluxes and velocities in each cell are updated. This iterative process then uses the updated pressure field to tabulate new pressure gradients and the whole procedure repeats until satisfactory convergence is achieved [20]. For each simulation evaluated over the course of this investigation, the model is terminated when the mass, momentum, and energy residuals drop below 10^{-9}. Additionally, facet minimum, maximum, and average trackers are applied to monitor the Nusselt number at the surface of the cylinder to ensure that the solution has converged.

In order to improve the convergence rate of the models, under-relaxation factors for the pressure and momentum calculations were altered to 0.70 and 0.30, respectively, while the remaining density and energy relaxation factors were left at the default values of unity. Gradients were treated with the usual Green-Gauss methodology which approximates the integral over a surface as a summation of the product of the average scalar value in each face and the face's surface vector. Second-order spatial discretization is utilized during the evaluation of the aforementioned energy and momentum conservation relationships.

3.6 HEAT TRANSFER PARAMETERS

To quantify the natural convection heat transfer from the surface of the confined cylinder, the Nusselt number, which is a dimensionless ratio of the convective to conductive heat transfer rates at a given surface, will serve as the chief metric throughout this analysis. A depiction of the complete horizontal cylinder with appropriate variable definitions to aid in the development of the Nusselt number is presented in Figure 7.

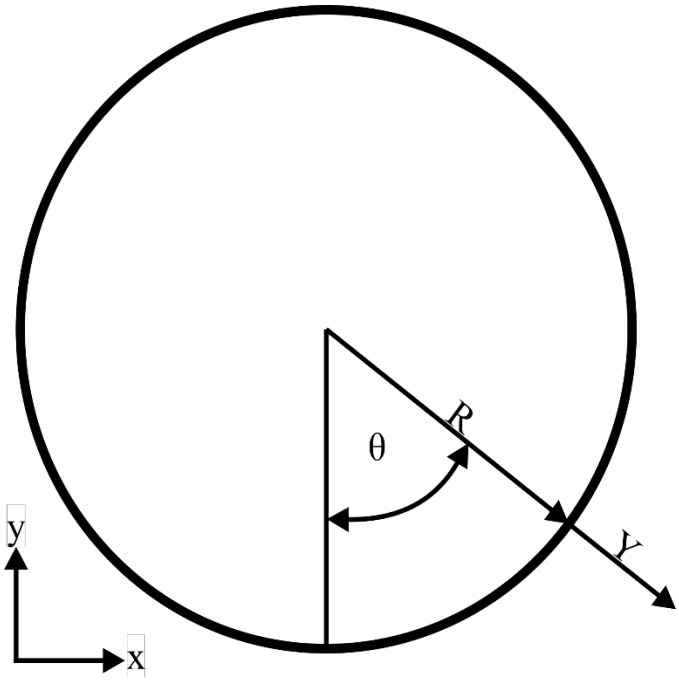

Figure 7: Depiction of cylinder geometry variables

Using the aforementioned relationship between Fourier's law of conduction and Newton's law of cooling at the surface of the cylinder allows for the formulation of the Nusselt number. Equating the convective and conductive heat transfer rates yields:

$$-kA\frac{\partial}{\partial Y}(T-T_s)\Big|_{Y=0} = h_\theta A(T_s - T_\infty) \tag{47}$$

where h_θ is the local convective heat transfer coefficient, A is the heat transfer area between the surface of the cylinder and the buoyancy-induced air flow region, and T_s is the local temperature at the surface of the cylinder at angle θ from the negative y-direction. Rearranging for the ratio of the convective heat transfer coefficient and the thermal conductivity of the fluid produces:

$$\frac{h_\theta}{k} = \frac{\frac{\partial}{\partial Y}(T_s - T)\Big|_{Y=0}}{(T_s - T_\infty)} \tag{48}$$

which can be made dimensionless by multiplying by a representative length. For the purposes of this investigation, the representative length was elected to be the diameter of the cylinder. Thus, the Nusselt number along the surface of the cylinder can be evaluated via:

$$\mathrm{Nu}_\theta = \frac{h_\theta D}{k} = \frac{\frac{\partial}{\partial Y}(T_s - T)\Big|_{Y=0}}{\frac{T_s - T_\infty}{D}} \tag{49}$$

When comparing the effective convective heat transfer resulting from the buoyancy-induced air flow regime across various confinement ratios and Rayleigh numbers, the facet-averaged Nusselt number provides a simpler avenue for assessment than its localized counterpart. Substituting the average convective heat transfer coefficient into Equation (49) allows for the calculation of the facet-average Nusselt number:

$$\mathrm{Nu}_\mathrm{D} = \frac{h_D D}{k} \tag{50}$$

By defining the Nusselt number as a single, averaged value across the diameter of the cylinder, the convective heat transfer rate can be easily compared across the two chief independent parameters of this investigation.

3.7 COMPUTATIONAL GRIDS

In order to determine the appropriate heat transfer parameters at the surface of the heated horizontal cylinder at various confinement ratios, computational finite-volume grids need to be generated for each desired geometrical configuration. To best capture the anticipated effect of the confinement on the relative heat transfer from the cylinder surface, 18 different ratios are selected in varying increments from 1.125 to 18.0. Since the evaluation of the buoyancy-induced flow regime at each

confinement ratio requires a unique geometry and computational grid, 18 distinct mesh files are constructed to be used in conjunction with the aforementioned computational model. In an effort to simplify the construction of each of these geometry and mesh files, the DesignModeler and Meshing packages in ANSYS's Workbench software are employed.

Starting from the rudimentary schematic present in Figure 6, the geometry for each selected confinement ratio is constructed parametrically using the DesignModeler software. To simplify the meshing procedure and to obtain a more structured computational grid, the geometry is then subdivided into smaller, more uniform regions. Figure 8 displays an example of this pre-processing geometry subdivision where the different colors specify the separation of adjacent regions.

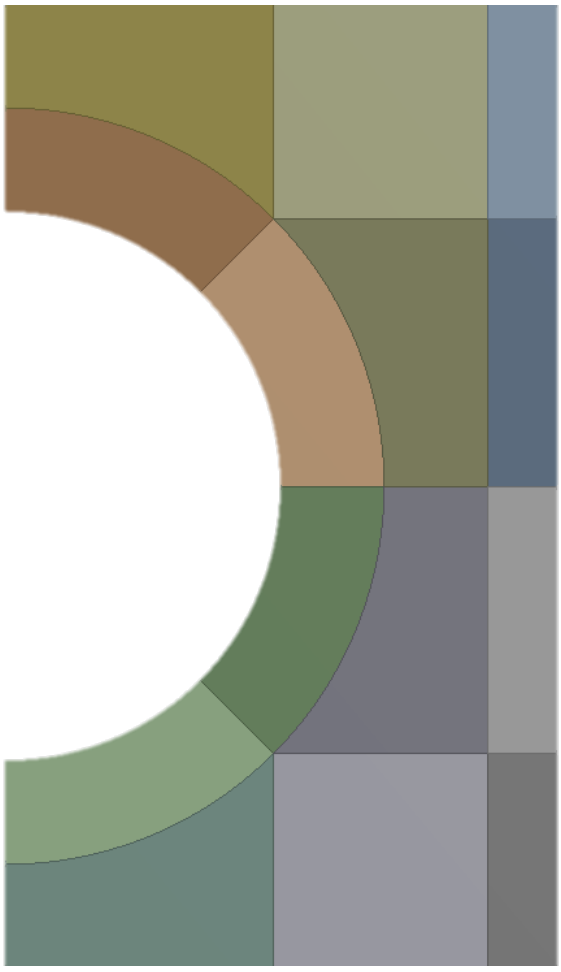

Figure 8: Example of pre-processing geometry subdivision (C = 2.0)

Following the creation and dissection of each of the 18 geometries, the ANSYS Meshing software is used to generate a structured grid that conforms to the boundaries of each region. In order to evaluate the effect spatial discretization plays on the numerical results obtained from each simulation, three different mesh files, with varying cell densities, are constructed for each of the 18 analyzed confinement ratios. Once the lowest density mesh is constructed, the ANSYS Meshing software is utilized to copy and refine the grid, producing a higher density network with four times more elements than the original mesh. Figure 9 displays the three different mesh densities generated for the geometry present in Figure 8 while Table 2 details the element counts for each of the 54 computational grids created throughout this investigation.

Table 2: Computational grid element counts for 18 analyzed confinement ratios

	Element Count		
Confinement Ratio	**Mesh #01**	**Mesh #02**	**Mesh #03**
1.125	46860	187440	749760
1.250	53560	214240	856960
1.375	56100	224400	897600
1.500	51600	206400	825600
1.625	60650	242600	970400
1.750	59410	237640	950560
1.875	59710	238840	955360
2.000	53750	215000	860000
2.500	60200	240800	963200
3.000	55200	220800	883200
3.500	55770	223080	892320
4.000	59750	239000	956000
5.000	54250	217000	868000
6.000	56450	225800	903200
8.000	51500	206000	824000
10.000	56350	225400	901600
12.000	59000	236000	944000
18.000	61300	245200	980800

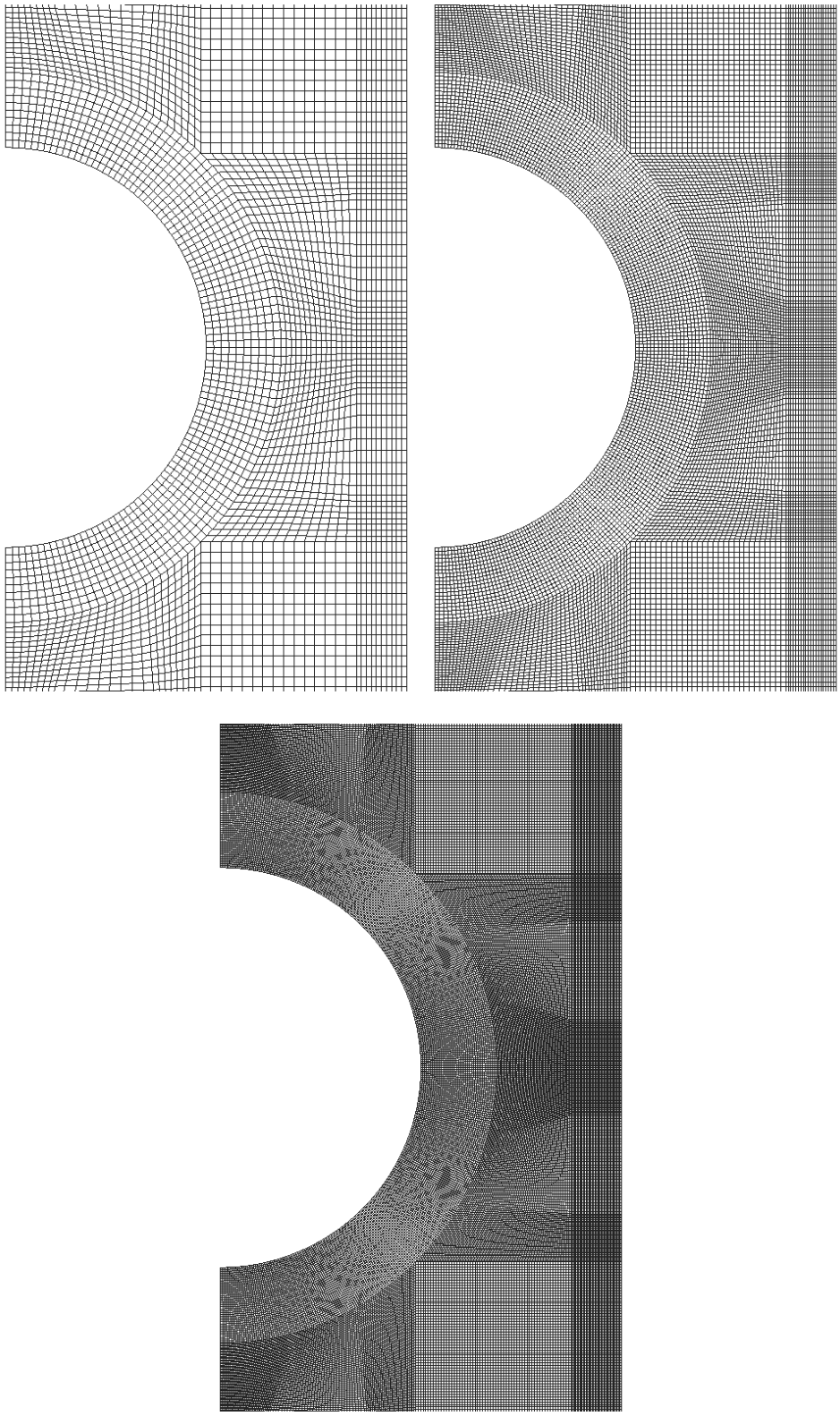

Figure 9: Low density (top left), medium density (top right), and high density (bottom) computational grids (C = 2.0)

3.7.1 Grid Independence Study

In order to evaluate the effect of computational mesh density on the heat transfer parameters obtained from each set of simulations, a grid independence study was conducted. Because of the computational resources available for this particular investigation, the goal of this preliminary analysis was to determine the necessity of the highest density computational grids. Taking only the bounding cases into consideration (lowest and highest Rayleigh numbers) for the smallest (C = 1.125) and largest (C = 18.0) domains allowed for a simple, effective metric by which to judge mesh independence. A thorough investigation of mesh independence for these extreme cases suggests that any other combination of independent parameters (C and $\mathrm{Ra_D}$) will be mesh independent as well. Through the use of a Delaunay interpolation scheme, field values at the cell centers of higher-density meshes can be compared to corresponding values on lower cell count grids.

Using the temperature and velocity fields as a point of comparison, contour plots of relative error between the medium and highest-density grids are created to display the effect mesh density plays on the simulations' results. Figure 10 and Figure 11 show archetypical relative percentage error contour plots for temperature and velocity magnitudes, respectively, between the two highest density computational meshes. These results are generated for a confinement ratio of 18.0 (note that the regions illustrated in Figure 11 and Figure 12 are only a small subset of the entire computational domain) and $\mathrm{Ra_D} = 10^5$. The maximum relative percent errors (2.31% and 0.31% for temperature and velocity, respectively) are indicative of each of the analyzed bounding cases and analogous results from the other extreme scenarios are congruent with the insignificant relative error present in Figure 11 and Figure 12. Based on the proximity of the results obtained from

higher density computational grids, grid independence has been achieved in the medium cell count meshes and subsequent refinement produces negligible accuracy improvement.

In addition to the comparisons of the temperature and velocity fields, linear profiles of a nondimensional temperature (ϕ), radial velocity (v_r'), and tangential velocity (v_θ') are compared across different computational grids. Each of these nondimensionalized parameters are defined via:

$$\phi = \frac{T(x,y) - T_\infty}{T_s - T_\infty}; \quad v_r' = \frac{v_r D}{\alpha}; \quad v_\theta' = \frac{v_\theta D}{\alpha}$$

Analogous to the contour plots of the temperature and velocity magnitude fields, each of the three nondimensional profiles show excellent convergence between the medium and high-density computational grids. This supports the previous conclusion that the medium density grid provides significant resolution of the physics within the channel around the central horizontal cylinder. A more detailed discussion of the nature of these profiles can be found in Section 4.0.

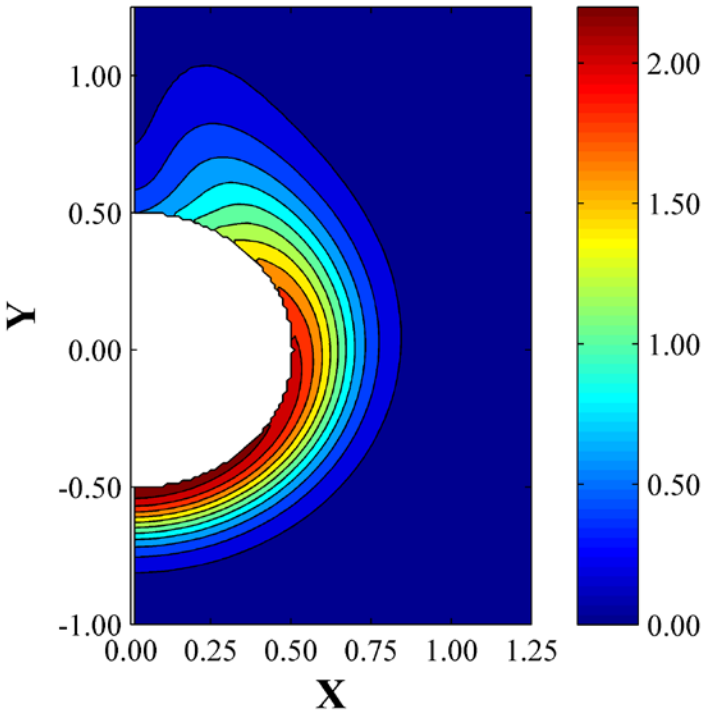

Figure 10: Relative error (%) between medium and high-density grids – temperature (C = 18.0, $\mathrm{Ra_D} = 10^5$)

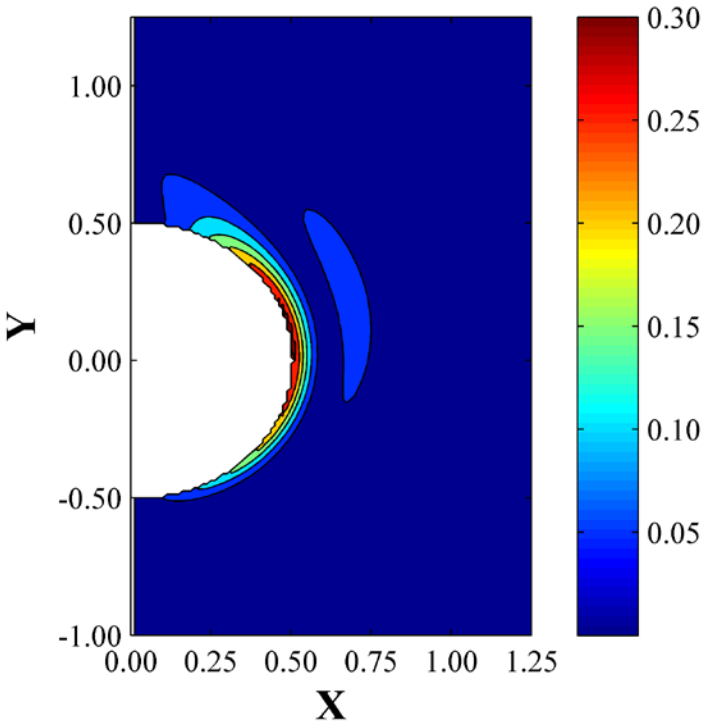

Figure 11: Relative error (%) between medium and high-density grids – velocity magnitude (C = 18.0, $\mathrm{Ra_D} = 10^5$)

4.0 UNCONFINED CYLINDER RESULTS

In order to evaluate the numerical results obtained from the aforementioned computational models, the data collected from the numerical simulations has been segregated into two collections: (1) pseudo-unconfined data from the highest confinement ratio (C = 18.0); (2) confined data from the remaining simulations. Based on the analytical derivations of [17], the numerical results obtained from the pseudo-unconfined case should be equivalent to similar computational methods evaluating fully-unconfined cylinders. This segregation of data will simplify the comparison and serve to isolate the physics unique to the confined scenarios.

4.1 UNCONFINED ISOTHERMAL CYLINDER

As natural convection heat transfer around an unconfined isothermal cylinder has been the subject of numerous investigations, the numerical data obtained from this investigation is compared to existing correlations to verify the validity of the computational models. For the purposes of this comparison, the computational models employing the largest confinement ratio, i.e., the scenarios most akin to fully-unconfined cylinders, are verified against previously established natural convection heat transfer correlations. Due to the assumptions made during the derivation of the energy equation (inclusion of the viscous dissipation of thermal energy) and the correlation's success in accurately representing empirical Nusselt numbers, the Fand and Brucker correlation from Equation (5) is employed to validate these results. Figure 12 displays the seven discrete average Nusselt numbers obtained from the largest confinement simulations along with a

continuous depiction of Equation (5). All seven of the Nusselt numbers obtained for this comparison fall within the 5% of the correlation proposed by Fand and Brucker and any discrepancy between the correlation and computational results can be primarily attributed to the neighboring confining walls.

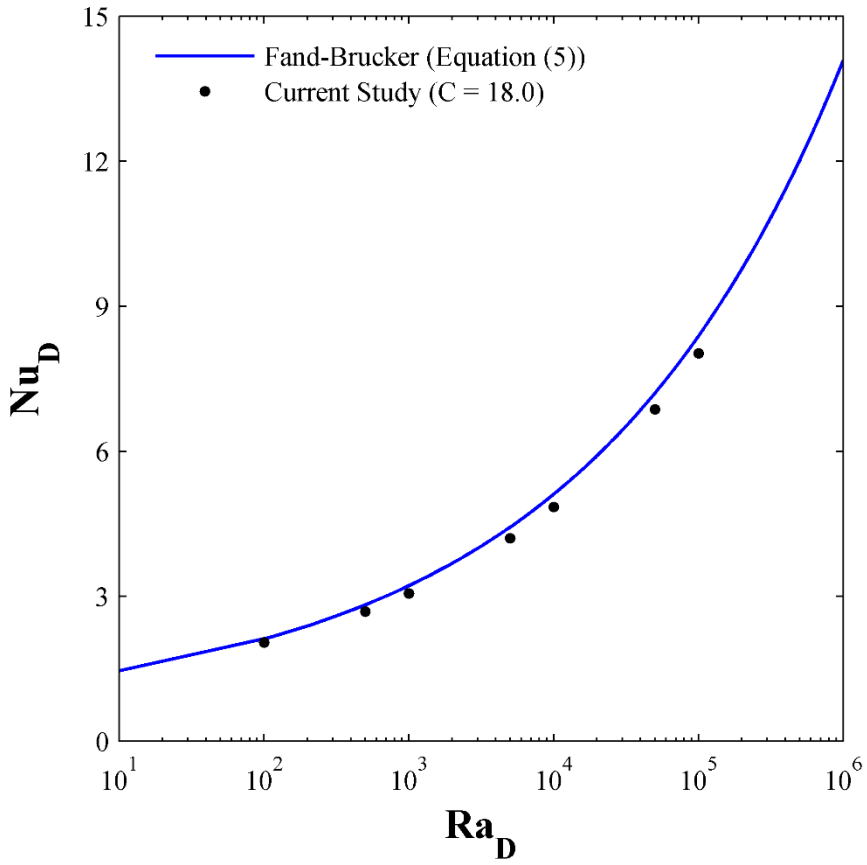

Figure 12: Average Nusselt number vs. Fand-Brucker correlation: isothermal cylinder (C = 18.0)

In addition to validating the average Nusselt numbers against documented heat transfer correlations, dimensionless temperature distributions normal to the pseudo-confined cylinder surface are constructed and compared against previous numerical investigations. Figure 13 and Figure 14 display dimensionless temperature distributions normal to the cylinder surface for Rayleigh numbers of 10^2 and 10^5, respectively.

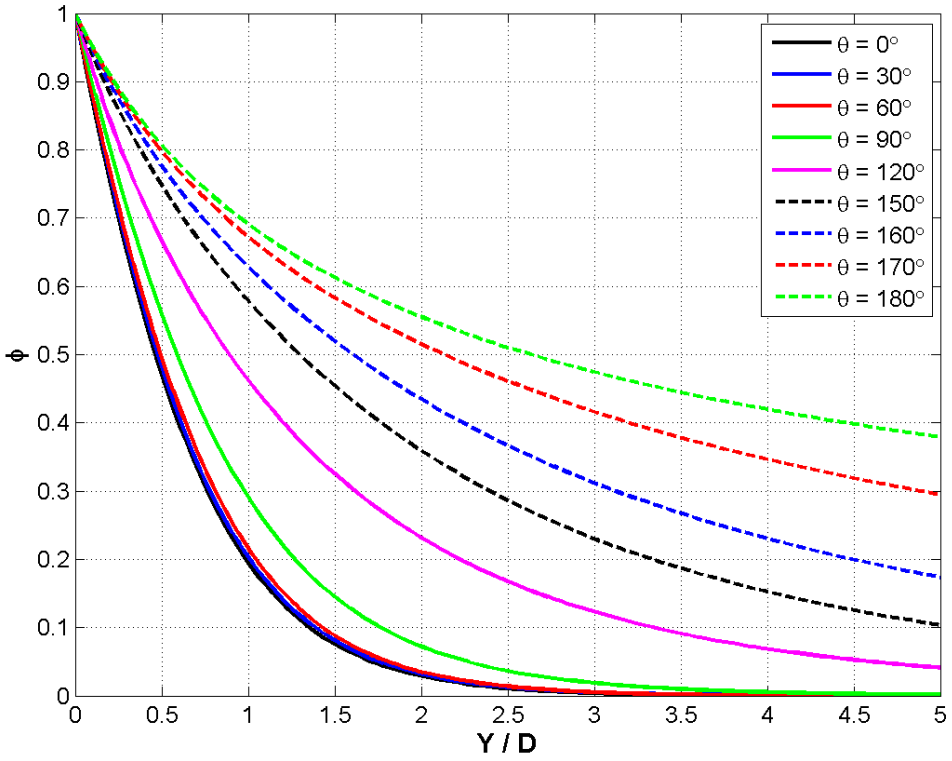

Figure 13: Dimensionless temperature profiles - isothermal (C = 18.0, $Ra_D = 10^2$)

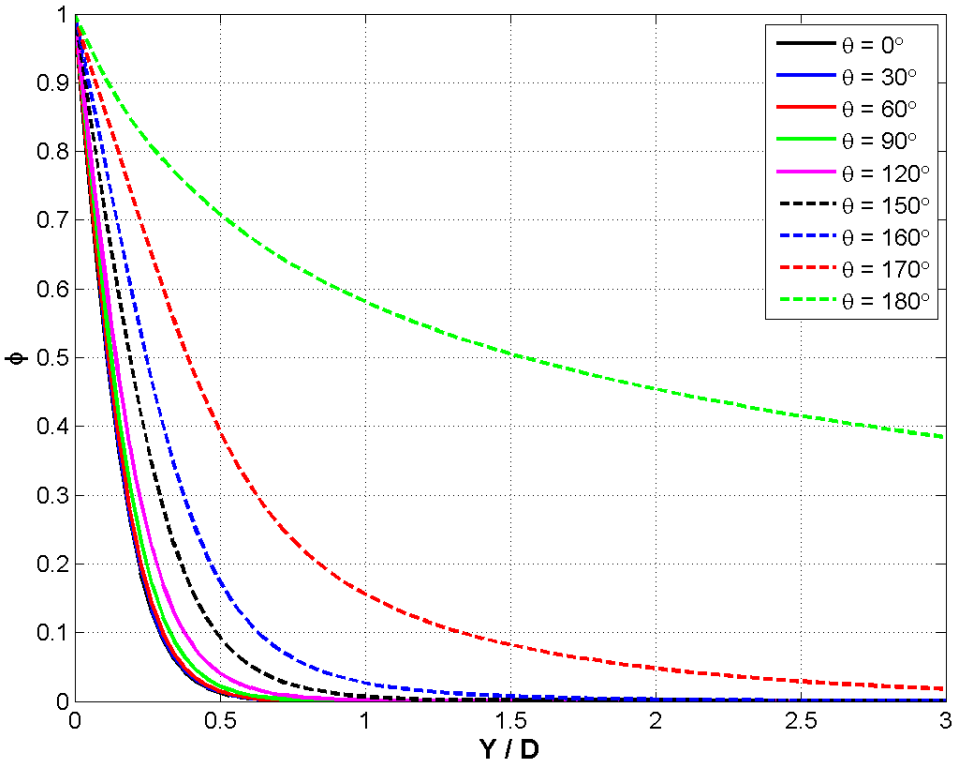

Figure 14: Dimensionless temperature profiles - isothermal (C = 18.0, $Ra_D = 10^5$)

Analyzing the dimensionless temperature distributions around the pseudo-unconfined isothermal cylinder reveals several interesting features about the nature of the buoyancy-induced flow. At the lowest Rayleigh number analyzed in this investigation ($Ra_D = 10^2$, Figure 13) thermal energy is convected in a well-defined plume as the temperature distributions resemble a line heat source. For a larger Rayleigh number ($Ra_D = 10^5$, Figure 14), the dimensionless temperature distributions reveal a transition to a boundary layer mode of heat transport [6]. Along the bottom half of the cylinder ($\theta < 90°$), the thermal boundary layer thickness is fairly uniform and is slightly smaller than the cylinder diameter. Between $90° < \theta < 150°$, the boundary layer thickens as the flow moves tangentially around the cylinder. At $\theta = 150°$, the dimensionless temperature raises significantly, indicating flow separation from the cylinder surface and plume formation. This transition to boundary layer heat transport can also be seen in contour representations of the dimensionless temperature in Figure 15 for $Ra_D = 10^2$ (left) and $Ra_D = 10^5$ (right).

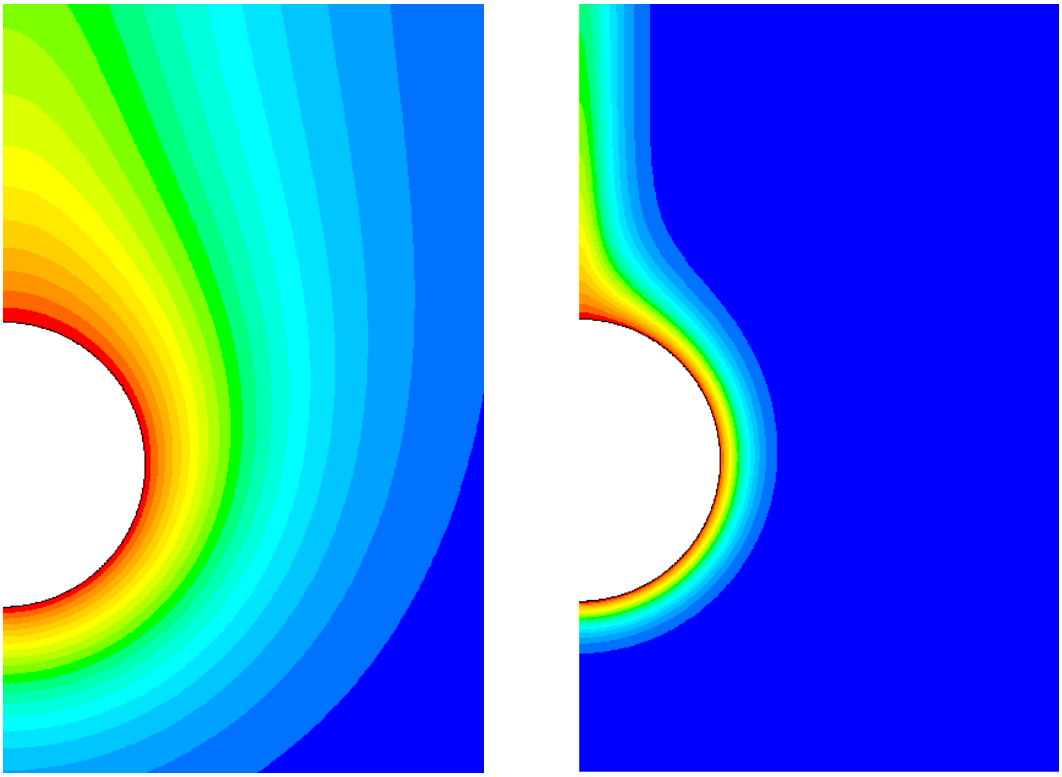

Figure 15: Dimensionless temperature contours - isothermal ($C = 18.0$, left: $Ra_D = 10^2$; right: $Ra_D = 10^5$)

Analogous to the work of [12, 13], radial and tangential velocity distributions normal to the surface of the cylinder can also be utilized to characterize the nature of the natural convection flow. For the lowest analyzed Rayleigh number (10^2), radial and tangential velocity distributions about the pseudo-unconfined isothermal cylinder are present in Figure 16 and Figure 18, respectively, while Figure 17 and Figure 19 display the same parameters for the highest analyzed Rayleigh number (10^5). Much like the higher Rayleigh number dimensionless temperature distribution from Figure 14, the radial velocities normal to the cylinder surface in Figure 17 also indicate separation and plume formation. For $0° < \theta < 120°$, the radial velocities are fairly small and the flow is moving rather uniformly towards the surface of the cylinder. However, between θ = 150° and 160°, the fluid changes directions from inflow to outflow, indicating a transition from boundary layer to plume flow [6]. This stark transition is not present at the lower Rayleigh number, but rather a more uniform increase in radial velocity is observed.

The thickness of the momentum boundary layer can be determined from the width of the tangential velocity peaks in Figure 18 and Figure 19. Unsurprisingly, the momentum boundary layer is approximately 30% smaller than the thermal boundary layer along the surface of the cylinder. Based on the definition and magnitude of the problem Prandtl number (Pr = 0.707), this result is anticipated. The magnitudes of both the radial and tangential velocity increase with increasing flow Rayleigh number due to the increased buoyancy force in the positive-y direction.

The dimensionless temperature and radial and tangential velocity distributions for the $Ra_D = 10^5$ case are compared against [6, 12, 13] to further validate the computational models employed during this study. Equivalent to the comparison of average Nusselt numbers from Figure 12, this assessment reveals congruency between current and previously established numerical results, confirming the validity of the FLUENT CFD models.

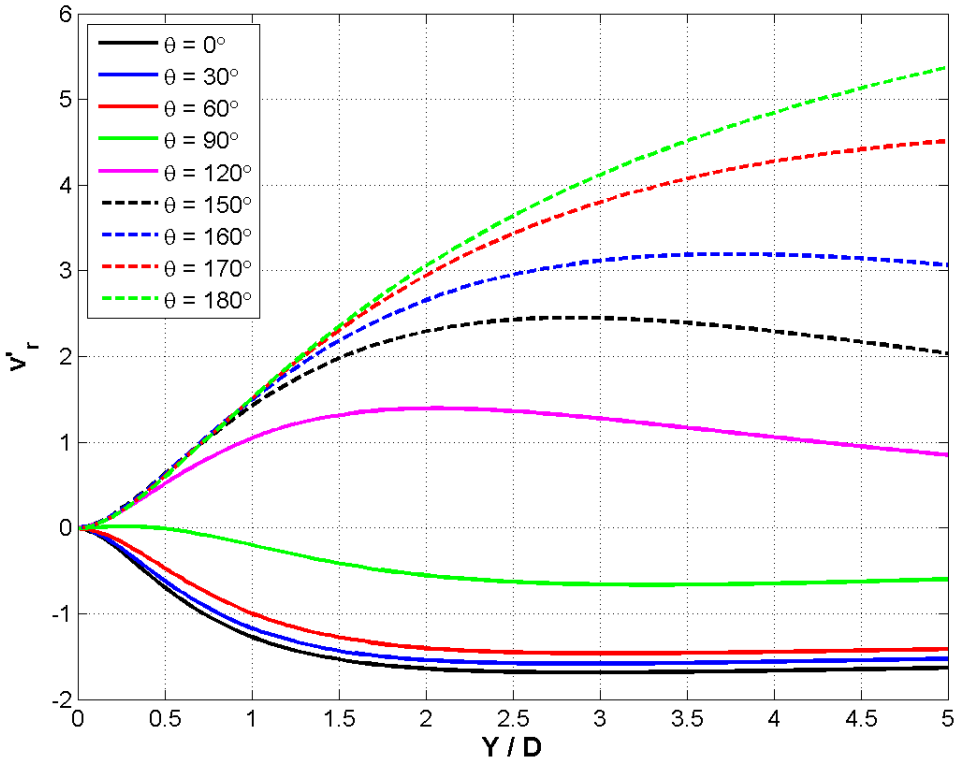

Figure 16: Dimensionless radial velocity profiles - isothermal (C = 18.0, $Ra_D = 10^2$)

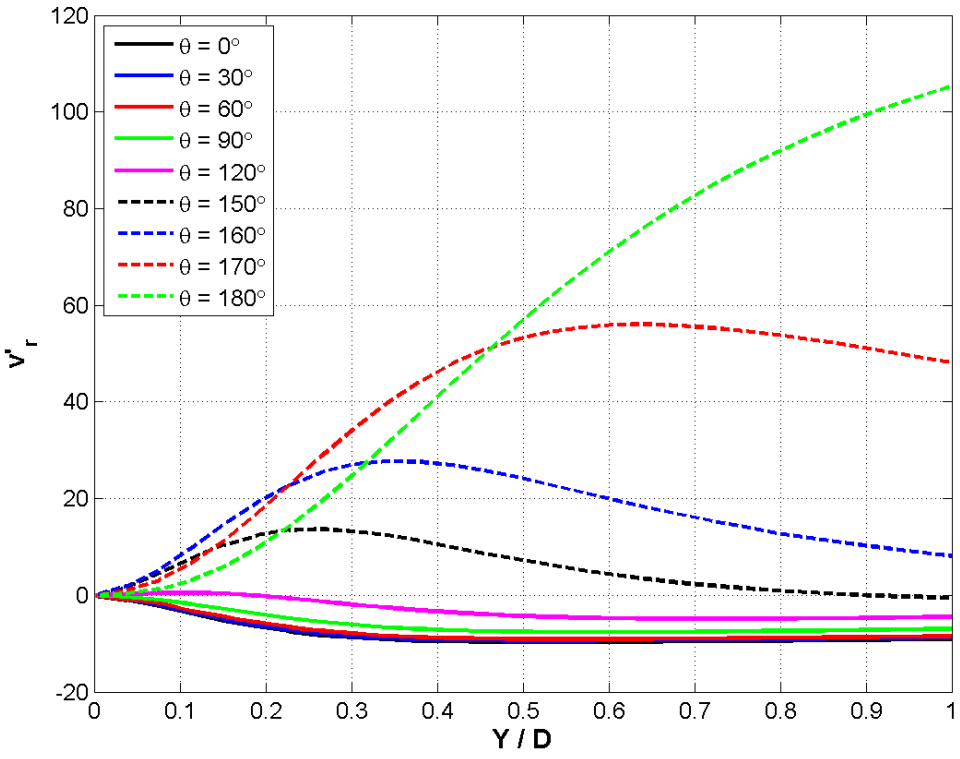

Figure 17: Dimensionless radial velocity profiles - isothermal (C = 18. 0, $Ra_D = 10^5$)

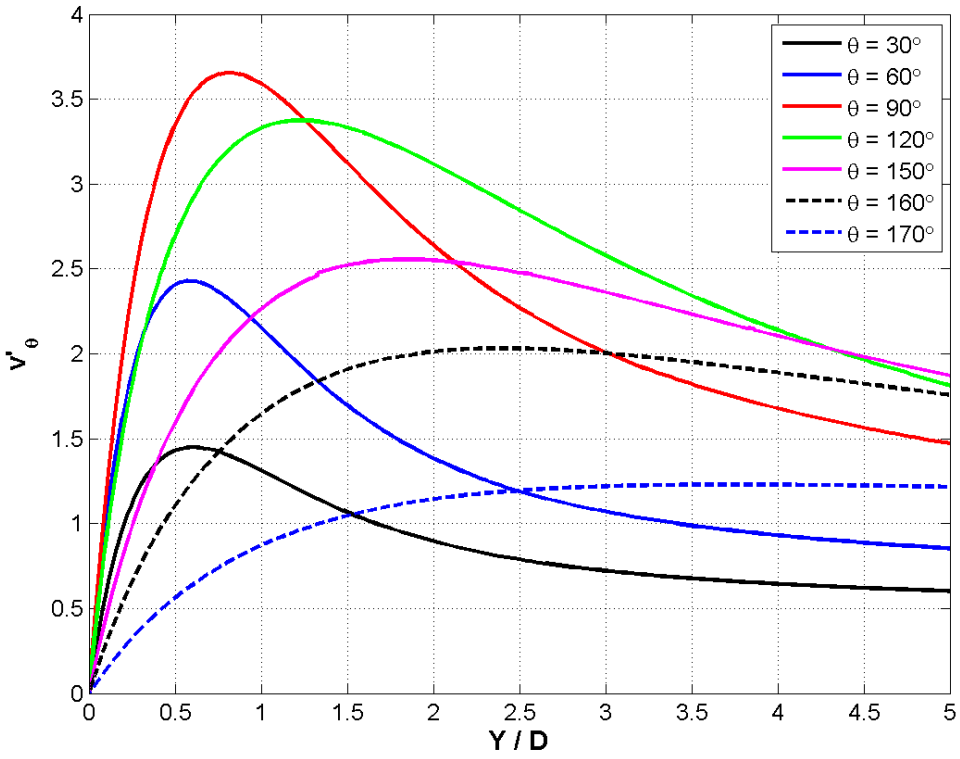

Figure 18: Dimensionless tangential velocity profiles - isothermal (C = 18.0, $Ra_D = 10^2$)

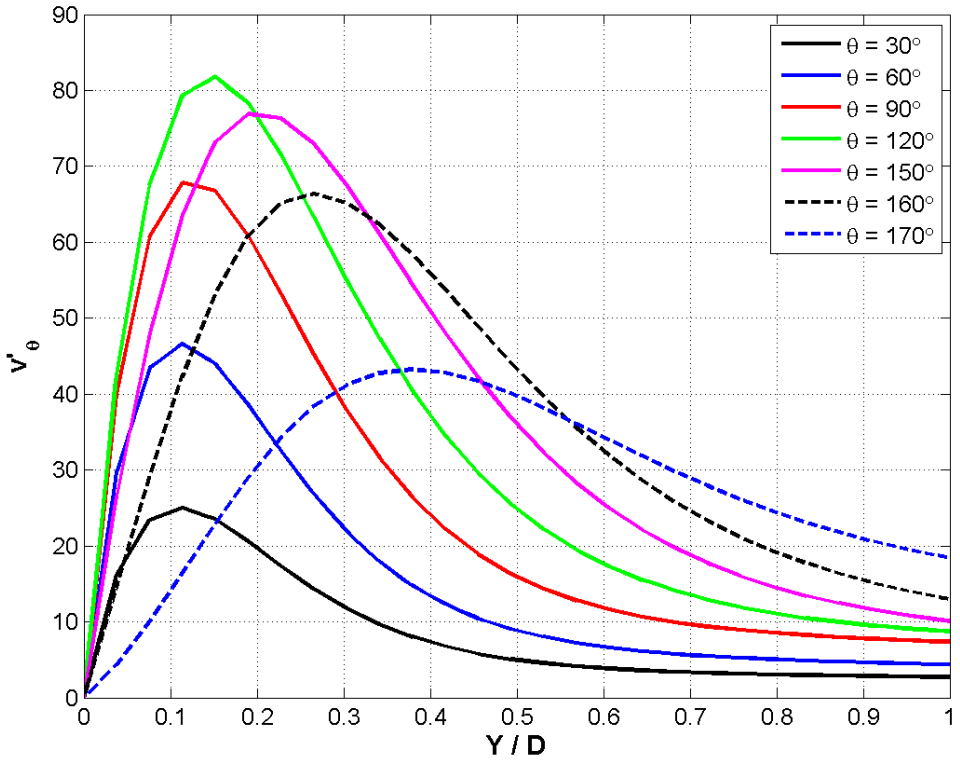

Figure 19: Dimensionless tangential velocity profiles - isothermal (C = 18.0, $Ra_D = 10^5$)

As shown by the dimensionless temperature distributions, the thermal boundary layer thickens as the flow moves tangentially along the surface of the heated cylinder. This will impact the local Nusselt number and have a degrading effect on the relative rate of heat rejection near the top of the cylinder. To illustrate this effect, Figure 20 displays local Nusselt numbers, normalized by the fourth root of the flow Rayleigh number, for each analyzed pseudo-unconfined computational model. As expected, the magnitude of the local Nusselt numbers increases with increasing Rayleigh number due to the increase in the buoyancy force acting on the fluid. For each curve shown in Figure 20, the local Nusselt number is also seen to decrease along the surface as the thermal boundary layer thickness increases. At the top of the cylinder (θ = 180°), the local Nusselt number reaches its minimum value as the boundary layers on the left and right halves of the cylinder collide to form the plume. All of these phenomenon are indicative of natural convection heat transfer from an unconfined cylinder.

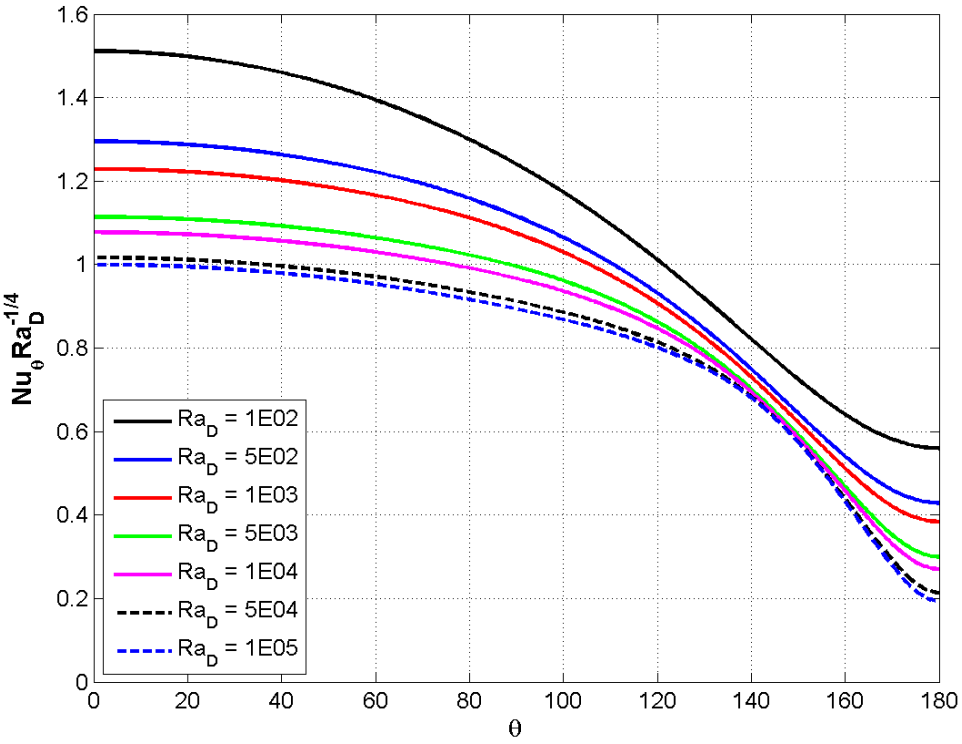

Figure 20: Local normalized Nusselt number – isothermal (C = 18.0)

4.2 UNCONFINED ISOFLUX CYLINDER

For the analysis of the pseudo-unconfined horizontal cylinder with the constant heat flux thermal boundary condition, the same three dimensionless parameters (temperature, radial velocity, and tangential velocity) were analyzed for each simulated modified Rayleigh number. Since the temperature along the surface of the cylinder is not known a priori for constant heat flux cases, a new, modified dimensionless temperature parameter, ϕ^*, is defined:

$$\phi^* = \frac{T - T_{min}}{T_s^* - T_{min}} \tag{51}$$

where T_s^* refers to the local cylinder surface temperature at angle θ and T_{min} is the minimum temperature along the projected surface normal vector at angle θ. The minimum temperature along the normal vector emanating from the cylinder surface was chosen to express ϕ^* in order to develop a consistent definition across all confinement ratios. Figure 21 and Figure 22 display modified dimensionless temperature distributions for $Ra_D^* = 10^2$ and $Ra_D^* = 10^5$, respectively. Figure 23 and Figure 24 portray the lowest and highest modified Rayleigh number radial velocity profiles, respectively, while Figure 25 and Figure 26 correspondingly depict the tangential velocities around the cylinder surface for these two cases. Finally, Figure 27 illustrates the local Nusselt number (Nu_θ^*), again normalized by the fourth root of the flux modified Rayleigh number, over each of the seven different discrete Ra_D^* values.

Comparing the pseudo-unconfined isothermal and isoflux dimensionless parameter profiles reveals little difference in terms of flow physics. For the flux modified dimensionless temperature distribution, the thermal boundary layer is slightly thicker than its isothermal counterpart, but there is no discernable difference in terms of profile shape. Additionally, both the radial and tangential velocity magnitudes are lower for the constant heat flux surface at each

analyzed angle, but the flow direction and transition from boundary layer to plume flow are consistent across both thermal boundary conditions. In order to quantify the difference between the two boundary conditions, the average Nusselt numbers for the pseudo-unconfined cases (Nu_D^*) are compared. Figure 28 displays the percent difference between the isothermal and isoflux average Nusselt numbers for each of the analyzed Rayleigh numbers. In this comparison, the difference between the isothermal and isoflux thermal boundary condition is proportional to the magnitude of the chosen Rayleigh number. As an example, for a modified Rayleigh number of 10^3, the anticipated surface average Nusselt number would be approximately 10% lower than an isothermal cylinder with the same magnitude Rayleigh number. Although the results only differ by a proportionality multiplier, there is still merit in evaluating the relative heat transfer rates from constant heat flux cylinders. Since dry cask designers will not know the surface temperature of their designs, a standard Rayleigh number cannot be calculated accurately. However, a modified Rayleigh number can be approximated by the amount of thermal energy in the loaded fuel assemblies and the size of the canister.

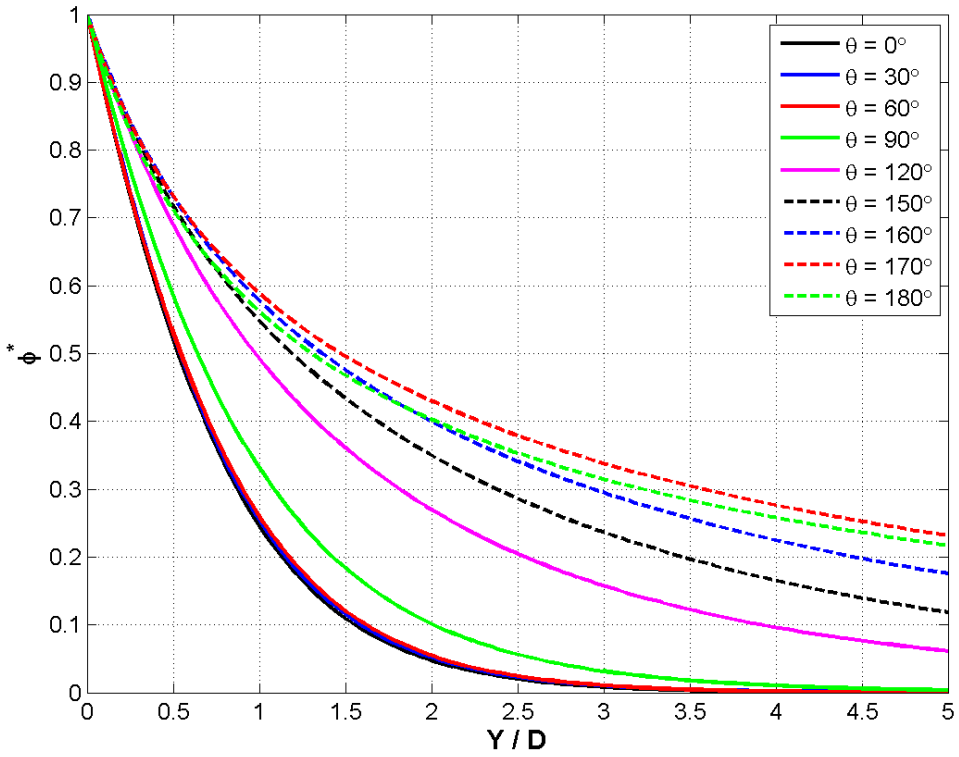

Figure 21: Dimensionless temperature profiles - isoflux (C = 18.0, Ra_D^* = 10^2)

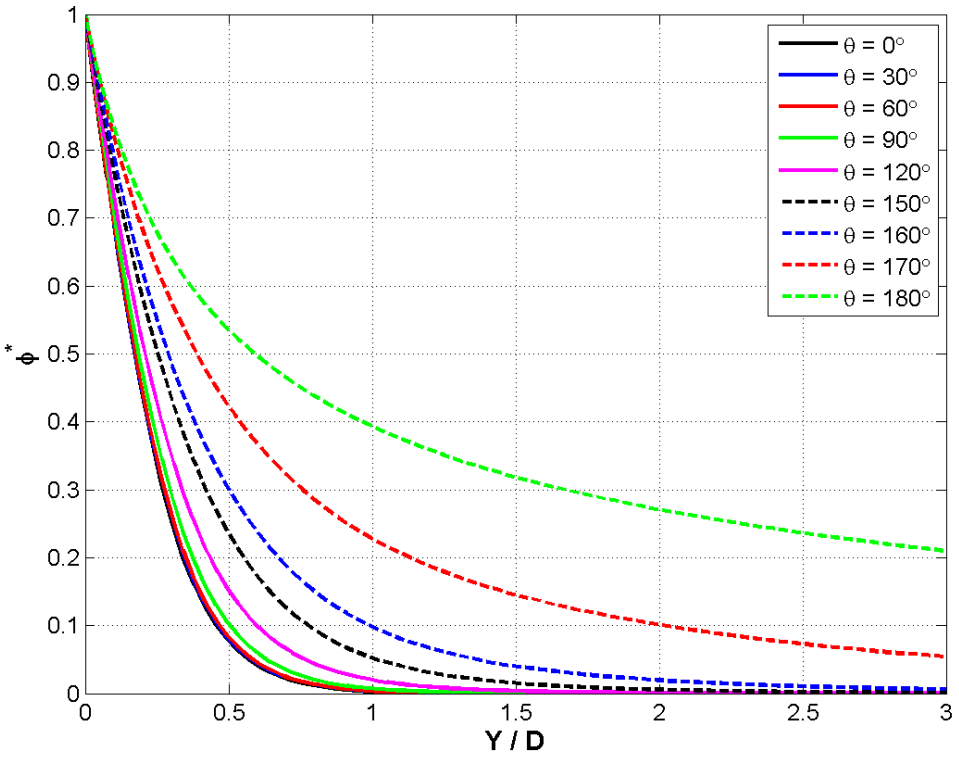

Figure 22: Dimensionless temperature profiles - Isoflux (C = 18.0, Ra_D^* = 10^5)

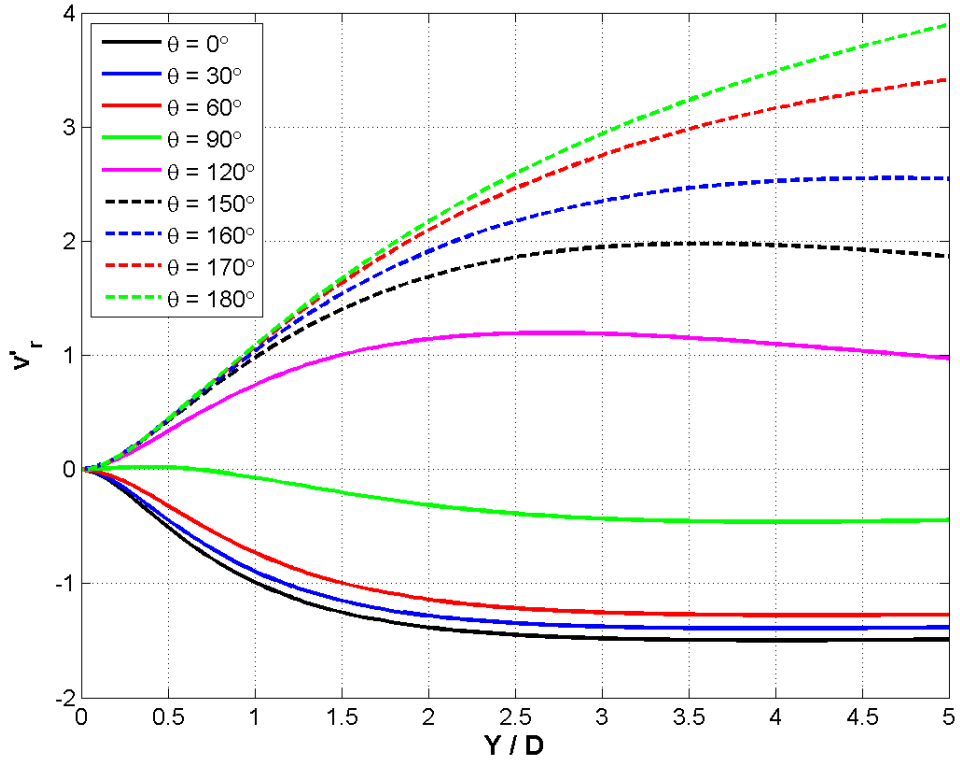

Figure 23: Dimensionless radial velocity profiles- isoflux (C = 18.0, Ra_D^* = 10^2)

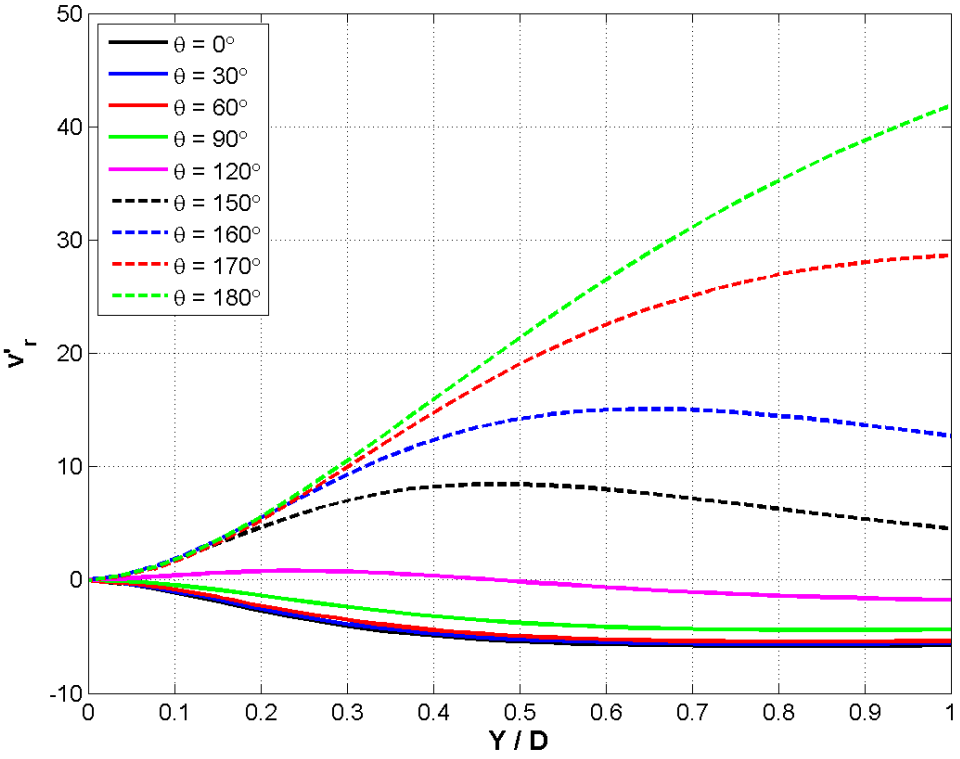

Figure 24: Dimensionless radial velocity profiles- isoflux (C = 18.0, Ra_D^* = 10^5)

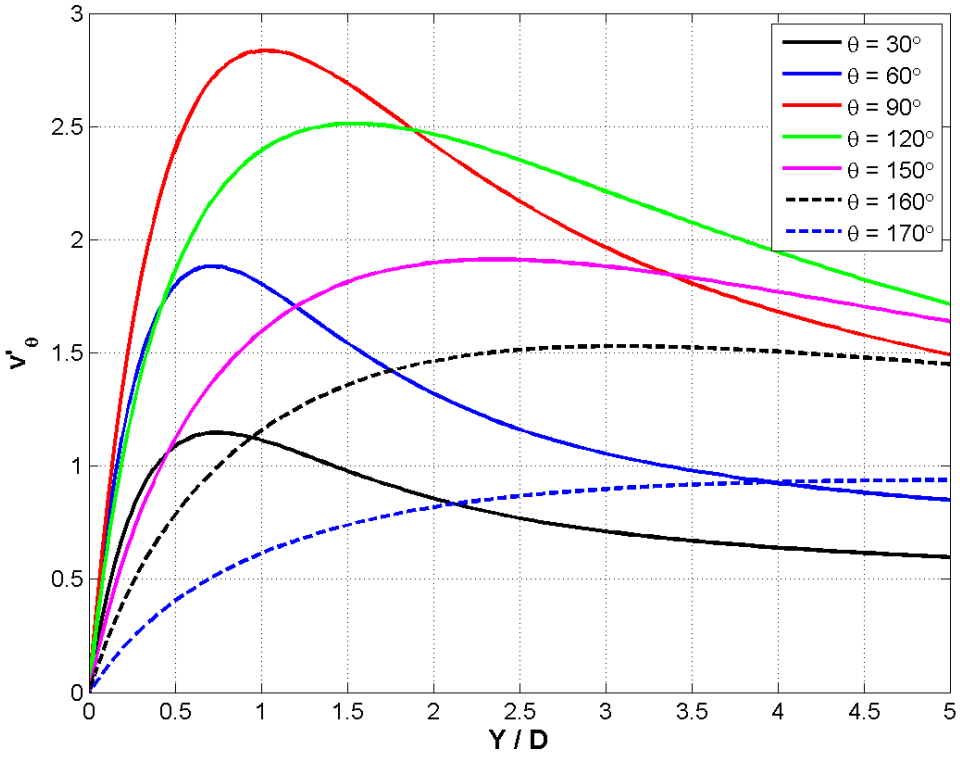

Figure 25: Dimensionless tangential velocity profiles - isoflux (C = 18.0, Ra_D^* = 10^2)

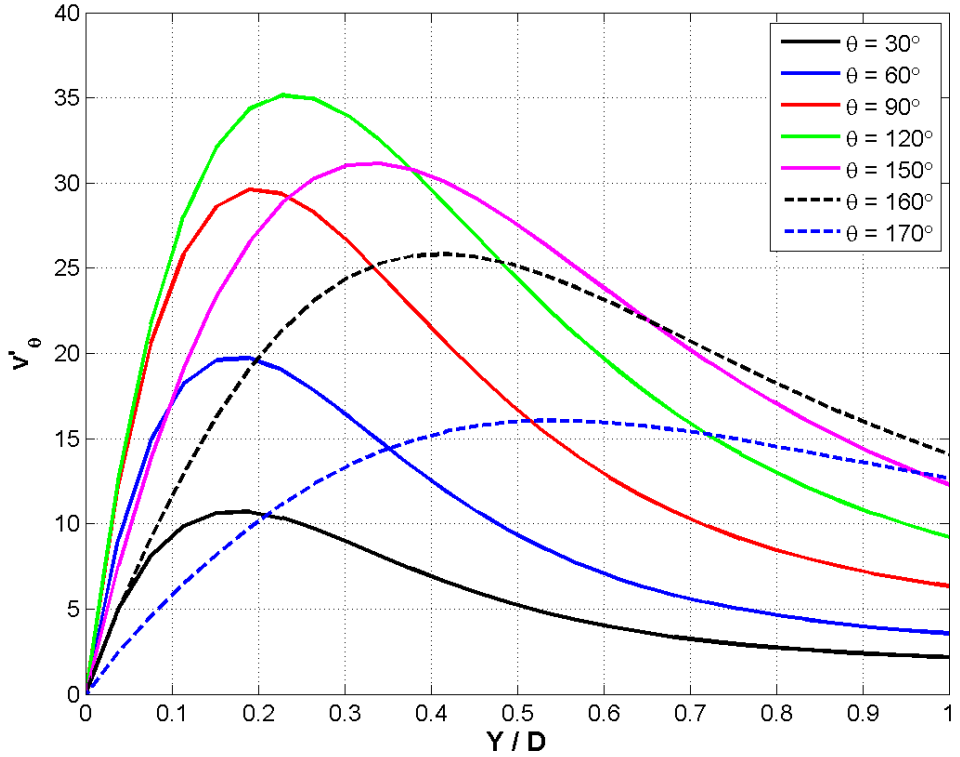

Figure 26: Dimensionless tangential velocity profiles - isoflux (C = 18.0, Ra_D^* = 10^5)

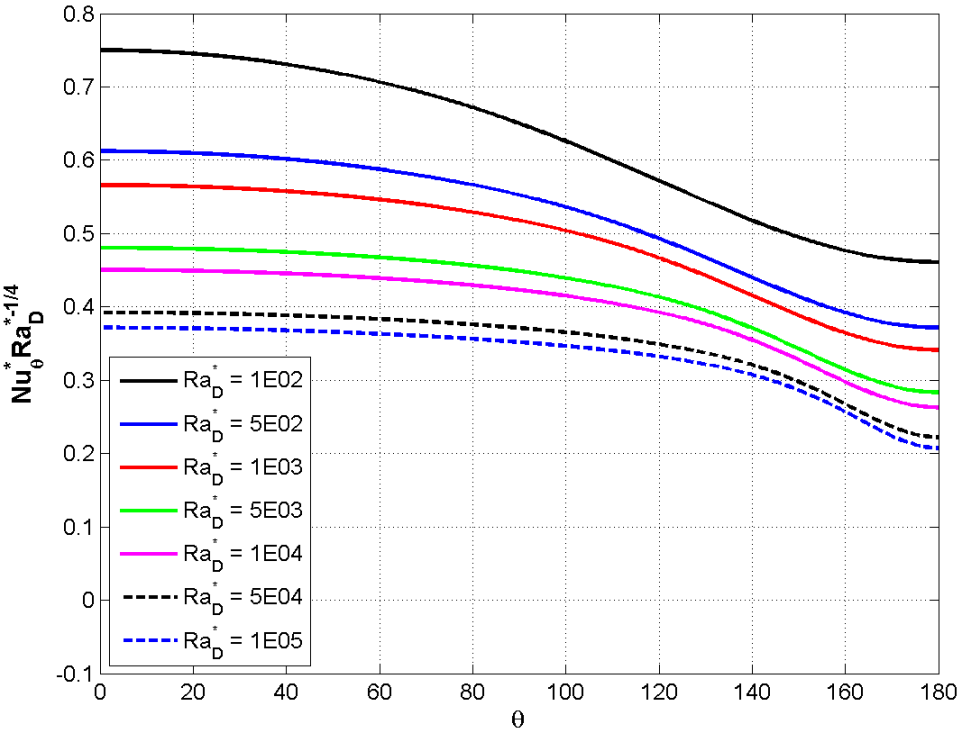

Figure 27: Local normalized Nusselt number – isoflux (C = 18.0)

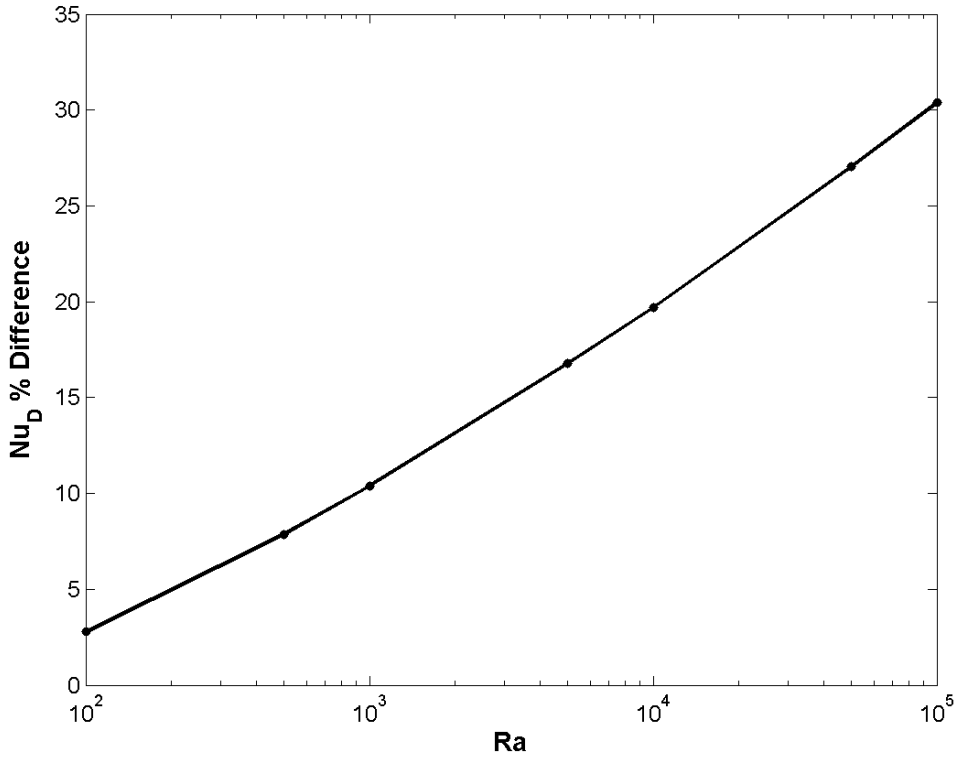

Figure 28: Nu_D – Nu_D^* percent difference comparison (C = 18.0)

5.0 EFFECT OF WALL CONFINEMENT

The second portion of the numerical data obtained from this investigation analyzes the effects of the confining walls on the rate of heat rejection from the surface of the heated cylinders.

5.1 ISOTHERMAL CYLINDER

With the computational models successfully validated against existing empirical and numerical fully-unconfined natural convection investigations, the effect of confinement on the heat transfer from the cylinder surface can be analyzed. As a starting point for this analysis, each of the 18 confinement ratios are evaluated over the previously established seven Rayleigh numbers to create a matrix of 126 average Nusselt numbers. Figure 29 displays the average Nusselt number at the cylinder surface over the 18 confinement ratios and seven analyzed Rayleigh numbers as evaluated on lowest density computational grids. Likewise, an analogous distribution of surface averaged Nusselt numbers for the medium density computational meshes is present in Figure 30.

Both distributions reveal local maximum average Nusselt numbers for each analyzed Rayleigh number at confinement ratios between 1.125 and 3.0. An asymptotic average Nusselt number is approached for each buoyancy condition as the confinement ratio is increased to the pseudo-unconfined state at 18.0. As previously mentioned, this type of behavior corresponds to the findings of [17] and reiterates the validity of approximating the largest confinement heat transfer parameters against unconfined heated cylinder correlations.

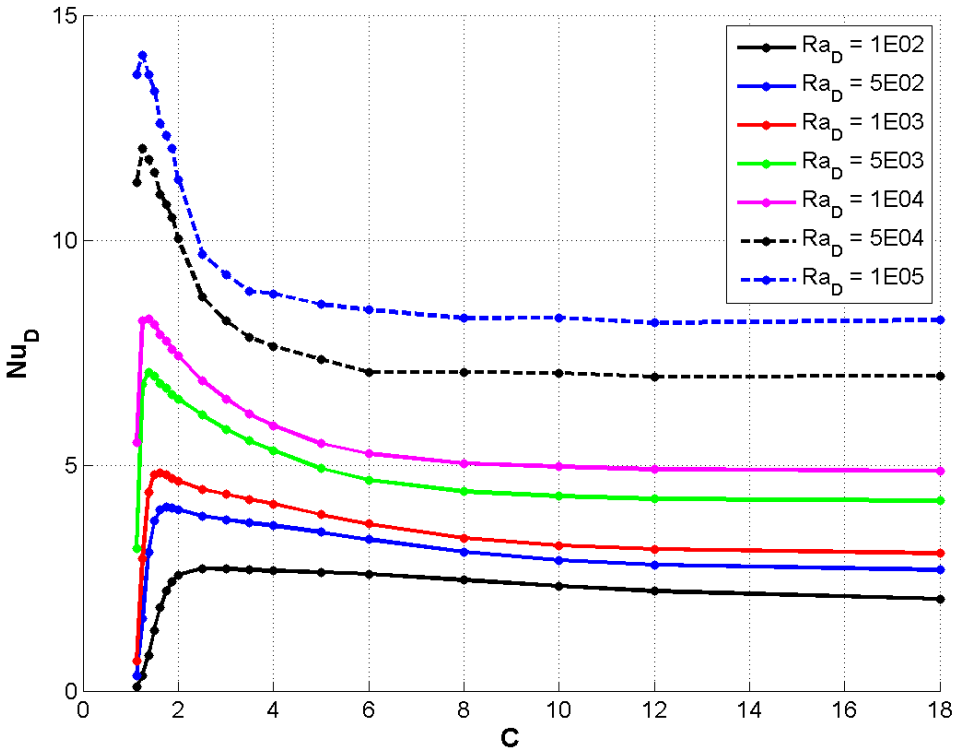

Figure 29: Average Nusselt number distribution – isothermal (low density mesh)

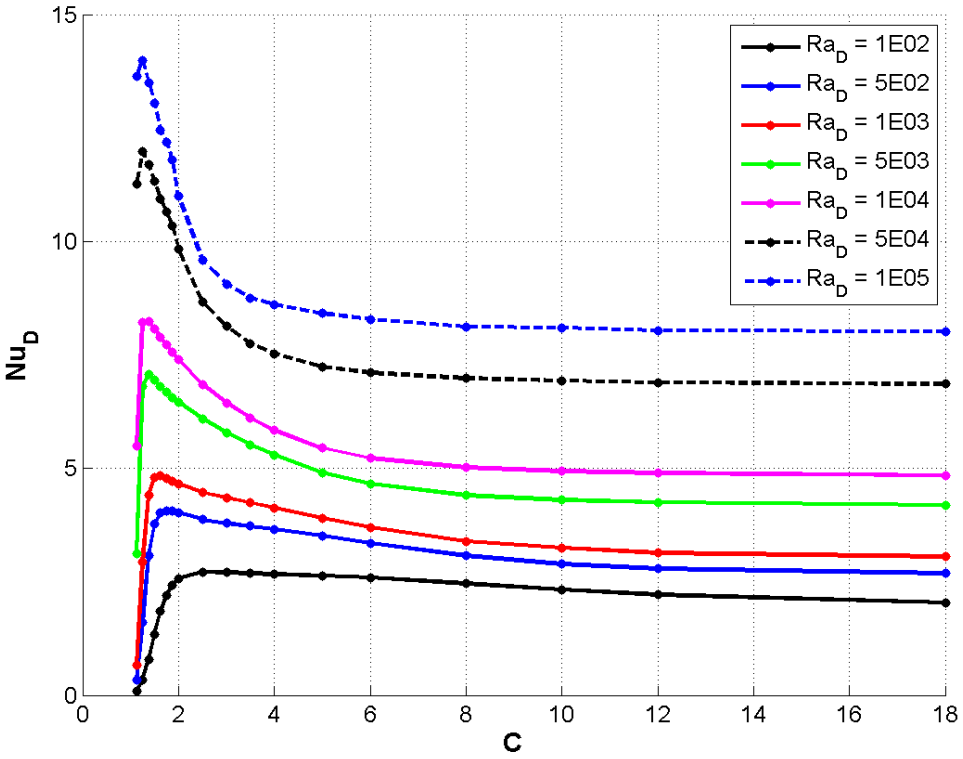

Figure 30: Average Nusselt number distribution – isothermal (medium density mesh)

Interestingly, the position of the local maximum shifts to lower confinement ratios with increasing flow Rayleigh number. This transition is due to a complex interaction between the formation and destruction of the thermal boundary layer around the cylinder surface and the buoyancy of the fluid. To illustrate this mechanism, take, for example, the local Nusselt number along the cylinder surface for $Ra_D = 10^5$ at various confinement ratios as depicted in Figure 31.

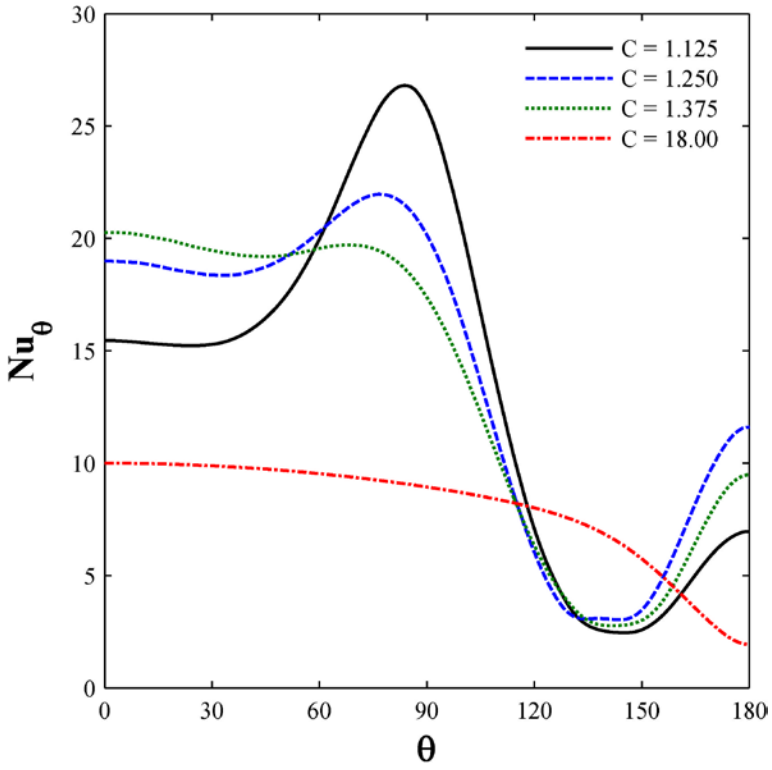

Figure 31: Local normalized Nusselt number – isothermal ($Ra_D = 10^5$)

For the three most confined cases (C = 1.125, 1.250, and 1.375), the local Nusselt number increases between $0° < \theta < 90°$ as the flow accelerates between the cylinder surface and confining wall. At $\theta = 90°$, the bolstered fluid velocity causes the bulk flow to separate from the cylinder, causing a dramatic decrease in the local Nusselt number between $90° < \theta < 150°$. The magnitude of the fluid velocity between the cylinder surface and confining wall creates a recirculation zone

atop the cylinder, which allows for fluid to reattach to the exterior of the cylinder at θ = 150° and reject additional thermal energy.

The complex behavior observed in the local Nusselt number profiles around the surface of the confined cylinder helps explain the physics of the buoyancy-induced flow, but does not solely explain the local maxima in the average Nusselt number. For this buoyancy condition, the maximum average Nusselt number occurs at a confinement ratio of 1.250. To better characterize the natural convection flow around the confined isothermal cylinders, three dimensionless temperature contours for confinement ratios of 1.125, 1.250, and 1.375 are presented in Figure 32.

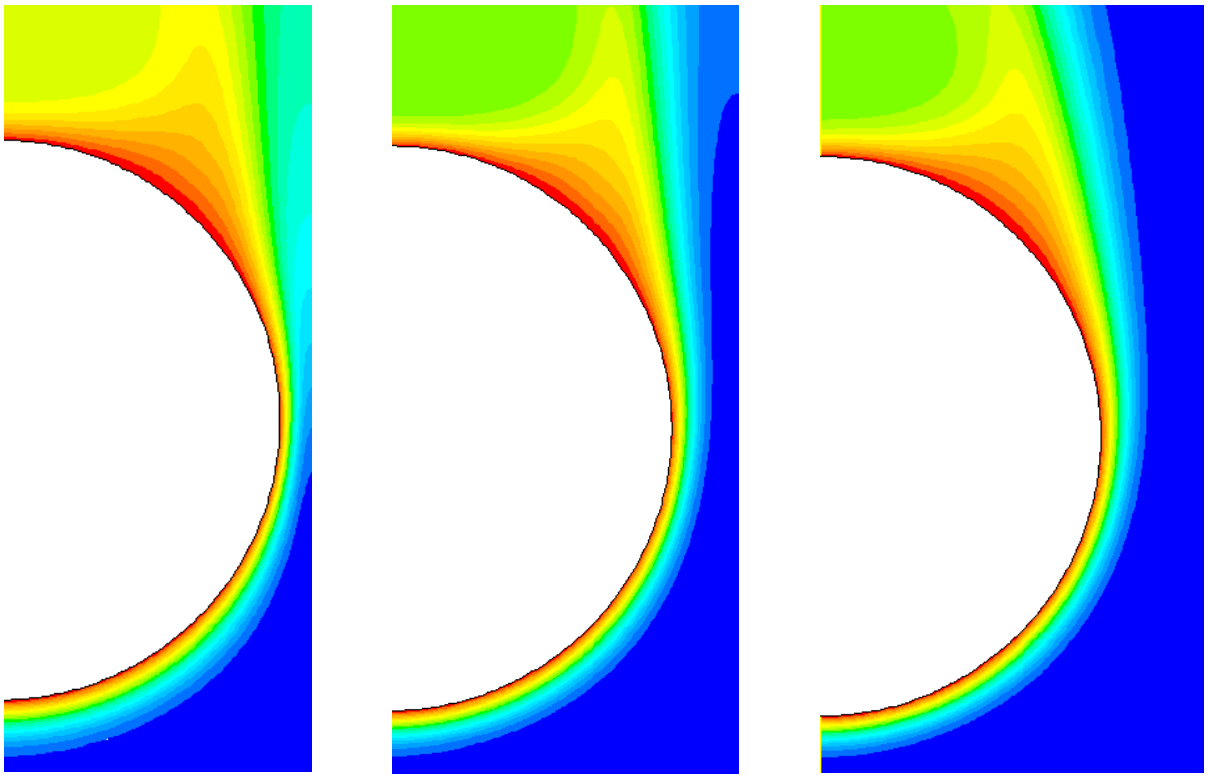

Figure 32: Dimensionless confined temperature contours – isothermal
($Ra_D = 10^5$, Left: C = 1.125; Center: C = 1.250; Right: C = 1.375)

The three dimensionless temperature contours reveal the fundamental cause of the local heat transfer maximum at the optimal confinement ratio. In the dimensionless temperature contour for C = 1.125, the confining wall restricts the development of the thermal boundary layer. Although

the tangential velocity of the fluid is highest for this case, it is not enough to overcome the detrimental effect of the confining wall on the average Nusselt number. Conversely, wall placement at C = 1.375 allows for the full development of the thermal boundary layer, but the flow is not constricted sufficiently to improve the local Nusselt number through the channel between the wall and side of the cylinder. Thus, the average Nusselt number is maximized at the smallest confinement ratio that does not constrict the development of the thermal boundary layer around the surface of the cylinder.

To characterize the optimal confinement ratio ($C_{Optimal}$) for each analyzed Rayleigh number, the following correlation is proposed between $10^2 < \mathrm{Ra_D} < 10^5$:

$$C_{Optimal} = 13.83\mathrm{Ra_D^{-0.5172}} + 1.218 \tag{52}$$

Analogous to the heat transfer correlation comparison made for the pseudo-unconfined isothermal cylinder, the proposed correlation is compared to the numerical results obtained throughout this investigation. Figure 33 displays the discrete optimal confinement ratios determined via the local maximums in Figure 30 alongside a continuous depiction of the proposed correlation from Equation (52).

Since the goal of this investigation is to maximize the amount of heat transfer from a confined horizontal canister filled with used fuel assemblies, an additional analysis was performed to quantify the improvement in the average Nusselt number relative to the pseudo-unconfined results. Figure 34 displays the percent improvement between the optimal average Nusselt number ($\mathrm{Nu_{D_{Optimal}}}$), or Nusselt number at the optimal confinement ratio, and the same parameter for the pseudo-unconfined cylinder. The magnitudes of the values present in Figure 34 reveal an improvement of 54.2% in the average Nusselt number at the highest Rayleigh number while a maximum improvement of 54.4% was observed at $Ra_D = 5 \times 10^4$.

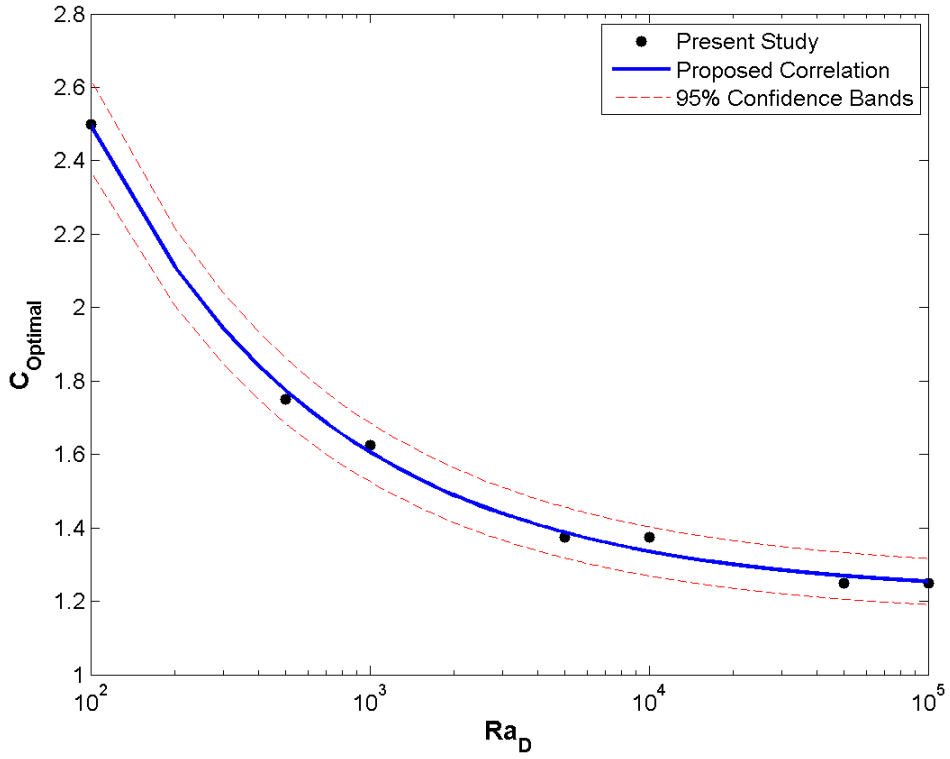

Figure 33: Optimal confinement ratio – isothermal

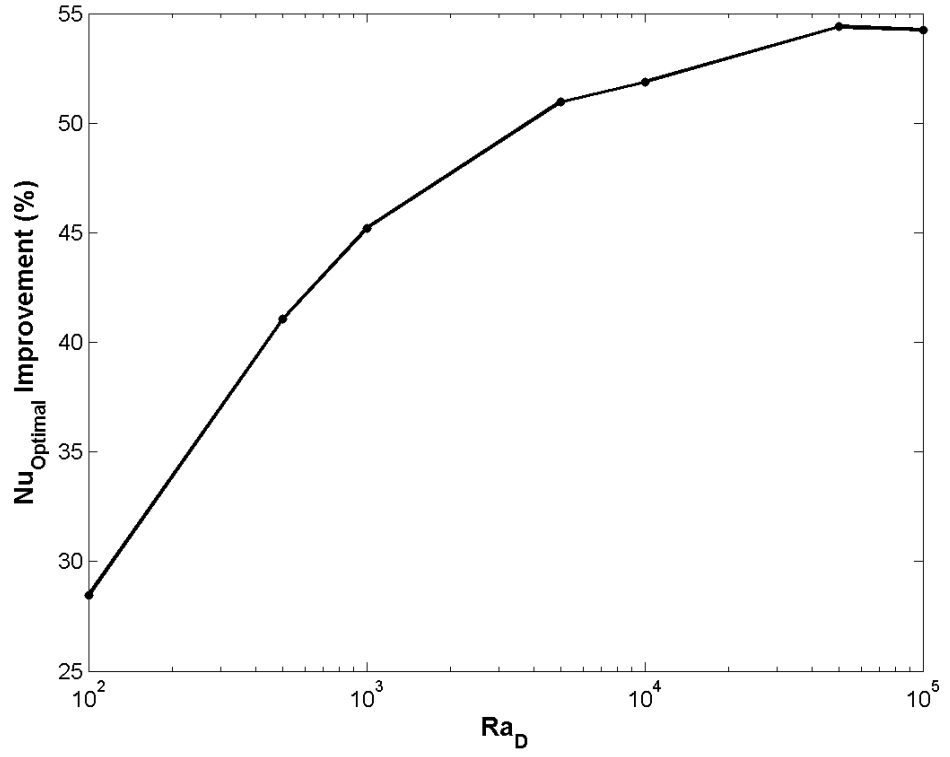

Figure 34: $Nu_{D\,Optimal}$ improvement relative to Nu_D

5.2 ISOFLUX CYLINDER

Much like the analysis of the confined isothermal horizontal cylinder, each of the 18 computational grids were evaluated at the seven flux modified Rayleigh numbers. Figure 35 displays the 126 different average Nusselt numbers obtained from the lowest density computational grids while Figure 36 depicts the Nu_D^* values obtained from the intermediate density meshes. Both Figure 35 and Figure 36 display lower average Nusselt numbers than their isothermal equivalents from Figure 29 and Figure 30, respectively. At each of the analyzed flux modified Rayleigh numbers, the optimal confinement ratio is slightly larger than the value obtained from same independent parameter combination in the isothermal computational models. Both of these facets are related to the aforementioned discrepancy between the standard and modified Rayleigh number. As evidenced by Figure 28, identical values of the standard and modified Rayleigh numbers produce different buoyant forces on the fluid. Thus, it is expected that the constant heat flux solutions will have larger thermal boundary layers, and, as a result, smaller average Nusselt numbers than the isothermal cases at Rayleigh numbers of equal magnitude.

For the constant heat flux thermal boundary condition, the following correlation is proposed to determine the optimal confinement ratio ($C_{Optimal}^*$) between $10^2 < Ra_D^* < 10^5$:

$$C_{Optimal}^* = 17.39 Ra^{*-0.5172}_D + 1.339 \quad (53)$$

To verify the correlation's estimated optimal confinement ratio against the numerical results of this investigation, Figure 37 employs 95% confidence bands around the values produced from Equation (53). Predictably, the numerical results fall within 5% of the proposed correlation values, indicating satisfactory precision between the two. Similarly, the improvement in the heat rejection from the confined constant heat flux cylinder can be evaluated to quantify the effect of the walls

on the surface Nusselt number. Figure 38 presents the percent difference between the isoflux optimal average Nusselt number ($Nu^{*}_{D_{Optimal}}$) and the same parameter for the pseudo-unconfined cylinder. The magnitudes of the values present in Figure 38 reveal an improvement of 46.6% in the average Nusselt number at the highest analyzed Rayleigh number while a maximum improvement of 46.8% was observed at $Ra^{*}_{D} = 5 \times 10^{4}$.

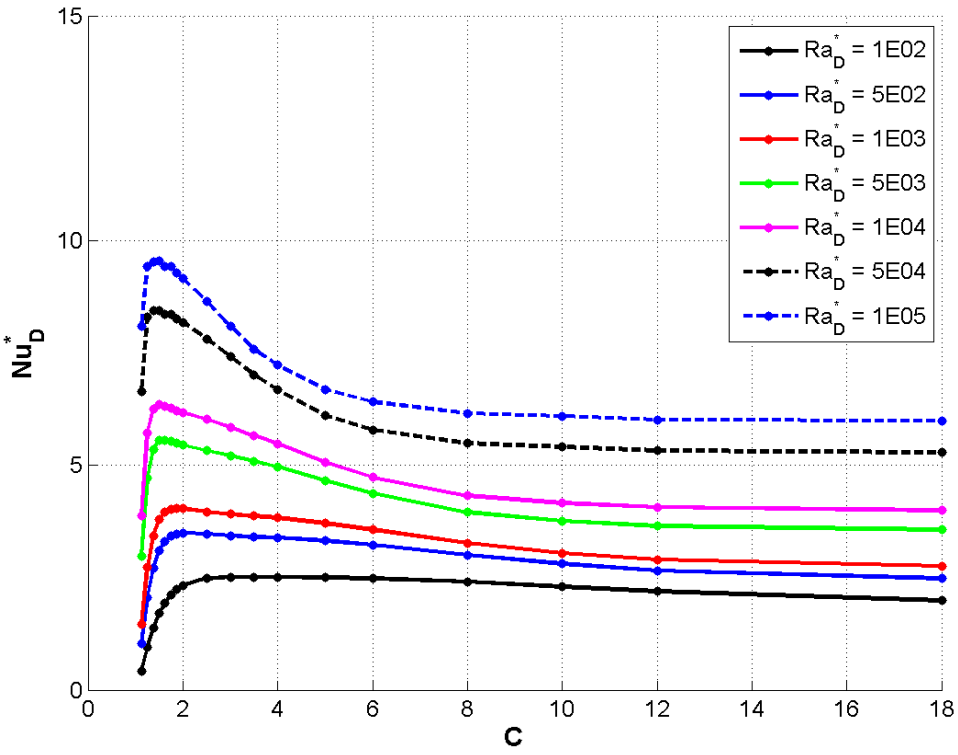

Figure 35: Average Nusselt number distribution – isoflux (low density mesh)

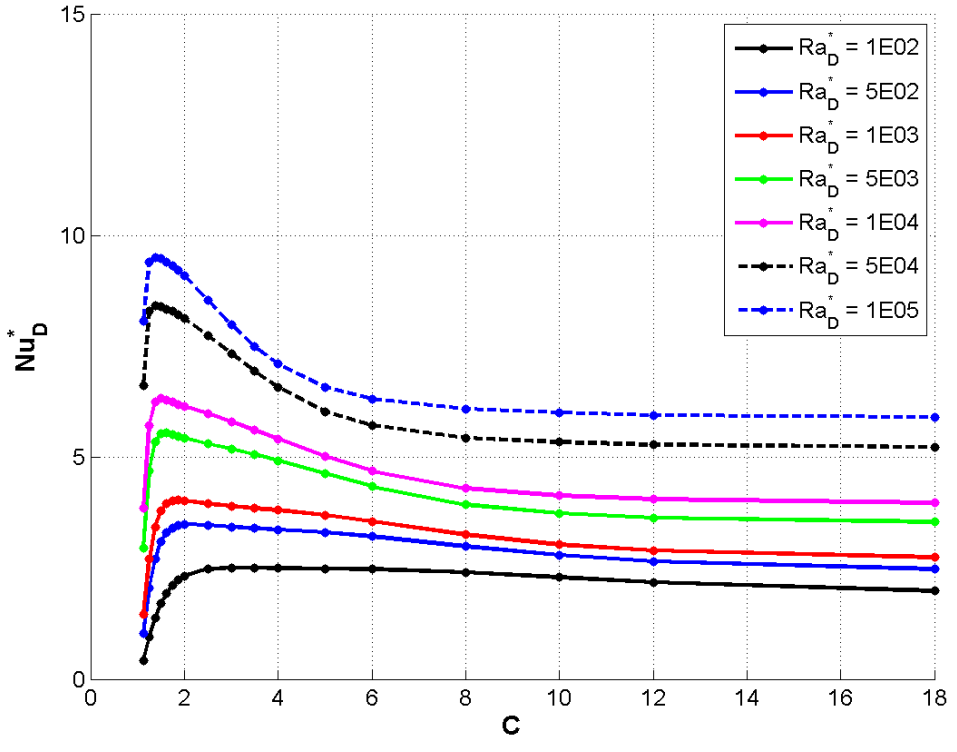

Figure 36: Average Nusselt number distribution – isoflux (medium density mesh)

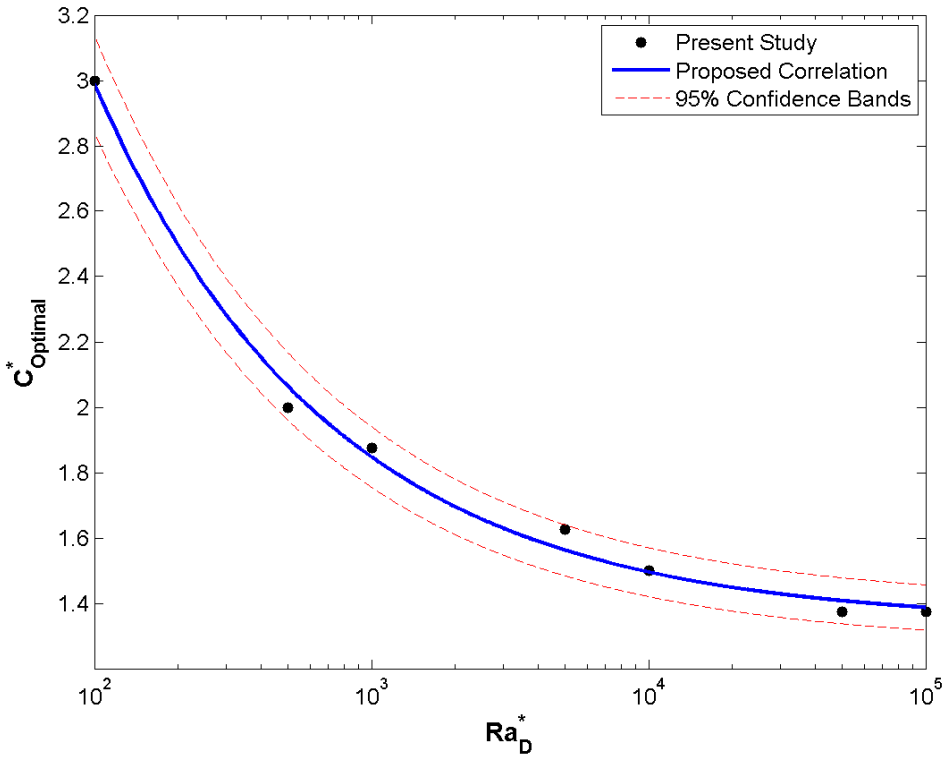

Figure 37: Optimal confinement ratio – isoflux

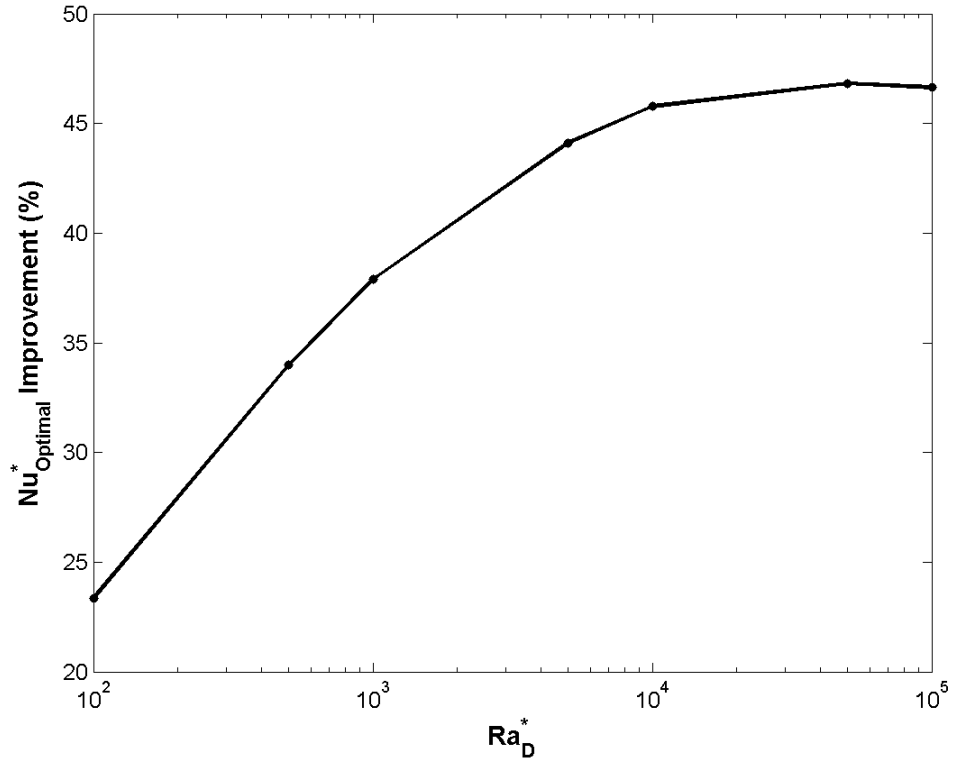

Figure 38: $Nu^*_{D_{Optimal}}$ Improvement Relative to Nu^*_D

6.0 CONCLUSIONS

The principal goal of this thesis was to focus on evaluating the fundamental physics associated with the buoyancy-induced flow around a confined heated horizontal cylinder. Numerical models were created and analyzed using the commercial FLUENT computational fluid dynamics software package at various combinations between $1.125 < C < 18.0$ and $10^2 < \mathrm{Ra_D} < 10^5$. The pseudo-unconfined heated isothermal cylinder results were found to agree well with both empirical correlations [11] and previous computational investigations [6, 12, 13]. Local Nusselt numbers around the surface of the pseudo-unconfined cylinder demonstrated the dependence of the heat rejection rate on the buoyancy of the fluid and position around the cylinder surface. For the confined analyses, maximum average Nusselt numbers were observed at an optimal confinement ratio for each analyzed Rayleigh number. When the flow is constricted below the optimal confinement ratio, the thermal boundary layer is disrupted as fluid travels through the channel between the cylinder surface and confining wall. Beyond the optimal confinement ratio, an unperturbed boundary layer can form around the cylinder, but fluid velocity is not bolstered adequately by the confining walls. Thus, the average Nusselt number is maximized at the smallest confinement ratio that does not hinder the development of the thermal boundary layer around the surface of the cylinder. Relative to the pseudo-unconfined cylinder at the largest confinement ratio, a 54.2% improvement in the heat transfer from an isothermal cylinder surface is observed at the optimum wall spacing for the highest analyzed Rayleigh number. Likewise, an analogous improvement of 46.6% is determined for the same conditions with a constant heat flux surface.

6.1 RECOMMENDATIONS

Moving forward, this investigation provides a critical first step in ultimately characterizing the buoyancy-driven convection around the internal canister of a horizontally-oriented dry cask storage system. Future computational efforts should focus on evaluating three-dimensional representations of confined heated horizontal cylinders at conditions more akin to those present in dry cask storage systems. A crucial component of any potential computational investigation will be to verify the simulation physics and chosen turbulence model against empirical data for these highly turbulent flows.

Another future investigation should focus on the development of correlations that describe the Nusselt number at the surface of the cylinder as a function of the defining Rayleigh number (Ra_D or Ra_D^*), the angular position along the surface, and the confinement ratio. By generating a single correlation centered on the three pertinent independent parameters, dry cask storage designers will be able to supply the relationship as a boundary condition for their finite-element representations of their canister designs. This will allow for an accurate determination of the fuel and internal component temperature distributions without having to perform a full-scale computational fluid dynamics simulation.

BIBLIOGRAPHY

[1] R. Alvarez, J. Beyea, K. Janberg, J. Kang, E. Lyman, A. Macfarlane, *et al.*, "Reducing the Hazards from Stored Spent Power-Reactor Fuel in the United States," *Science and Global Security*, vol. 11, pp. 1-51, 2003.

[2] I. Torres, "Nuclear Watchdog Approves Removal of Fuel Rods from Fukushima Reactor," in *Japan Daily Press*, 1st ed, 2013.

[3] "Final Safety Analysis Report for the Standardized NUHOMS Horizontal Modular Storage System for Irradiated Nuclear Fuel," Transnuclear Inc., Hawthorne, NY, 2004.

[4] M. A. McKinnon and M. E. Cunningham, "Dry Storage Demonstration for High-Burnup Spent Nuclear Fuel - Feasibility Study," Pacific Northwest National Laboratory, 2003.

[5] Z. Xu, M. S. Kazimi, and M. J. Driscoll, "Impact of High Burnup on PWR Spent Fuel Characteristics," *Nuclear Science and Engineering*, vol. 151, pp. 261-273, 2005.

[6] B. Gebhart, Y. Jaluria, R. L. Mahajan, and B. Sammakia, *Buoyancy-Induced Flows and Transport*. New York: Hemisphere Publishing Corporation, 1988.

[7] W. H. McAdams, *Heat Transmission*, 3rd ed. New York: McGraw-Hill Book Company, Inc., 1954.

[8] V. T. Morgan, "The Overall Convective Heat Transfer from Smooth Circular Cylinders," *Advances in Heat Transfer*, vol. 11, pp. 199-264, 1975.

[9] S. W. Churchill and H. H. S. Chu, "Correlating Equations for Laminar and Turbulent Free Convection from a Horizontal Cylinder," *International Journal of Heat and Mass Transfer*, vol. 18, pp. 1049-1053, 1975.

[10] R. M. Fand, E. W. Morris, and M. Lum, "Natural Convection Heat Transfer from Horizontal Cylinders to Air, Water, and Silicone Oils for Rayleigh Numbers Between 3 x 10^2 and 2 x 10^7," *International Journal of Heat and Mass Transfer*, vol. 20, pp. 1173-1184, 1977.

[11] R. M. Fand and J. Brucker, "A Correlation of Heat Transfer by Natural Convection from Horizontal Cylinders that Accounts for Viscous Dissipation," *International Journal of Heat and Mass Transfer*, vol. 26, pp. 709-716, 1983.

[12] T. H. Kuehn and R. J. Goldstein, "Numerical Solution to the Navier-Stokes Equations for Laminar Natural Convection About a Horizontal Isothermal Circular Cylinder," *International Journal of Heat and Mass Transfer*, vol. 23, pp. 971-979, 1980.

[13] B. Farouk and S. I. Güçeri, "Natural Convection from a Horizontal Cylinder - Laminar Regime," *Journal of Heat Transfer,* vol. 103, pp. 522-527, 1981.

[14] G. F. Marsters, "Natural Convection Heat Transfer from a Horizontal Cylinder in the Presence of Nearby Walls," *The Canadian Journal of Chemical Engineering,* vol. 35, pp. 144-149, 1975.

[15] B. Farouk and S. I. Güçeri, "Natural and Mixed Convection Heat Transfer Around a Horizontal Cylinder Within Confining Walls," *Numerical Heat Transfer,* vol. 5, pp. 329-341, 1982.

[16] M. S. Sadeghipour and S. K. Hannani, "Transient Natural Convection from a Horizontal Cylinder Confined Between Vertical Walls - A Finite Element Solution," *International Journal for Numerical Methods in Engineering,* vol. 34, pp. 621-635, 1992.

[17] M. S. Sadeghipour and Y. P. Razi, "Natural Convection from a Confined Horizontal Cylinder: The Optimum Distance Between the Confining Walls," *International Journal of Heat and Mass Transfer,* vol. 44, pp. 367-374, 2001.

[18] C. E. Clifford, M. L. Kimber, and J. D. Metzger, "Preliminary CFD Analysis of High-Thermal Capacity Dry Storage Systems," presented at the American Nuclear Society: 2013 Annual Meeting, Atlanta, GA, 2013.

[19] S. V. Patankar, *Numerical Heat Transfer and Fluid Flow,* 1st ed.: Taylor & Francis, 1980.

[20] R. H. Pletcher, J. C. Tannehill, and D. A. Anderson, *Computational Fluid Mechanics and Heat Transfer,* 3rd ed. Hoboken, NJ: Taylor and Francis, 2012.